Mathematical Biosciences 370 (2024) 109168

Contents lists available at ScienceDirect

Mathematical Biosciences

journal homepage: www.elsevier.com/locate/mbs

Original research article

Selected aspects of avascular tumor growth reproduced by a hybrid model of cell dynamics and chemical kinetics

Marco Scianna

Department of Mathematical Sciences, Politecnico di Torino, Corso Duca degli Abruzzi 24, 10129 Torino, Italy

ARTICLE INFO

MSC:
92C17
92C32
92C42
92C50

Keywords:
Tumor invasion
Individual-based model
Hybrid model
Tumor morphology

ABSTRACT

We here propose a hybrid computational framework to reproduce and analyze aspects of the avascular progression of a generic solid tumor. Our method first employs an individual-based approach to represent the population of tumor cells, which are distinguished in viable and necrotic agents. The active part of the disease is in turn differentiated according to a set of metabolic states. We then describe the spatio-temporal evolution of the concentration of oxygen and of tumor-secreted proteolytic enzymes using partial differential equations (PDEs). A differential equation finally governs the local degradation of the extracellular matrix (ECM) by the malignant mass. Numerical realizations of the model are run to reproduce tumor growth and invasion in a number scenarios that differ for cell properties (adhesiveness, duplication potential, proteolytic activity) and/or environmental conditions (level of tissue oxygenation and matrix density pattern). In particular, our simulations suggest that tumor aggressiveness, in terms of invasive depth and extension of necrotic tissue, can be reduced by (i) stable cell–cell contact interactions, (ii) poor tendency of malignant agents to chemotactically move upon oxygen gradients, and (iii) presence of an overdense matrix, if coupled by a disrupted proteolytic activity of the disease.

1. Introduction

Solid tumors typically arise from small nodes of cells of a given organ or tissue, subjected to genetic mutations and/or epigenetic alterations. These damage agents, able to escape from DNA repair mechanisms, acquire over time further malfunctions, that allow them an uncontrolled proliferation and the possibility to survive in harsh conditions [1,2]. The primary lesion undergoes an early phase of aberrant growth, which results in the consumption of chemical critical substrates: the surrounding environment, in particular the existing vasculature, is in fact often inadequate to supply and deliver a sufficient amount of nutrients and growth factors [3–5]. A necrotic core indeed emerges in the central and more dense area of the malignancy, formed by individuals dead for deprivation of vital substances.

To avoid the same fate, the remaining fraction of viable cells starts to release pro-angiogenic factors to drive a sort of malignant vascularization i.e., the formation of a functional micro-circulatory system around the lesion by extension of capillaries from the main vascular network. The disease can indeed further progress and even infiltrate blood and lymphatic vessels by cells with the potential to establish satellite clusters in distant parts of the host body [6]. These new colonies may finally begin to grow to form secondary lesions. This phenomenon, termed *metastatization*, drastically reduces the survival possibility of the patient, as the efficacy of most therapeutic interventions strongly decreases [7,8].

Malignant angiogenesis is not the only mechanism that promotes metastatic processes. Before vascular transition, a tumor can in fact infiltrate the surrounding host, as well as nearby tissues, by formation and/or extension of invasive structures, that range from dispersed groups of agents to compact fronts of malignant mass. The aggressiveness of the lesion in this phase is typically determined by the biophysical characteristics of its component cells. For instance, malignancies with the highest invasive potential mainly consist of cells with enhanced mesenchymal traits, i.e., poor adhesiveness, high motility and ability to secrete matrix degrading enzymes (MDEs) [9,10]. On the opposite, more treatable diseases are formed by cells with typical epithelial determinants, such as low migratory capacity and high tendency to form stable contact junctions. The internal composition of a tumor can vary during its progression spontaneously and/or in response to environmental conditions. A malignant mass can be also considered as an evolving ecosystem, whose component individuals compete for space and resources under selective pressures but also collaborate to maximize their survival potential [11].

In the last decades a fundamental help in cancer research is provided by the *mathematical modeling*, able to realistically reproduce selected features of the biological system and to test potential therapeutic strategies. Theoretical methods in this field can be distinguished, in a first approximation, in *continuous* and *discrete* approaches.

E-mail address: marco.scianna@polito.it.

https://doi.org/10.1016/j.mbs.2024.109168
Received 4 September 2023; Received in revised form 10 February 2024; Accepted 23 February 2024

The former group of models is characteristic of a macroscopic point of view and based on principles from continuum mechanics. They use partial differential and/or integro-differential equations to reproduce the spatio-temporal evolution of cancer-related variables, such as local amounts of malignant (and non-malignant) cells, extracellular matrix (ECM) components, matrix-degrading enzymes (MDEs), nutrients, and/or growth factors.

In continuous approaches, the tumor aggregate is typically treated as a fluid [12–15] or as an element with a different biomechanical nature (e.g., elastic/hyperelastic [16–19], poroelastic [20], viscoelastic [21,22], or elasto-viscoplastic [23]) and subjected to internal and external forces. Cell movement is then incorporated through diffusion [24–27], convection [28–30], taxis-like dynamics [31–35], or by the use of the Darcy's law [14,36–38], the Stokes equations [39–41], or the Darcy-Stokes (Brinkman) equations [42]. Continuous models are also suitable to include cell proliferation and death, that are usually set to depend on the interactions of the malignant mass with the surrounding environment [12,20,22,28,30,37,39,40,43–46], and angiogenic processes [45,47–51].

Multiphase models are a widely-used type of continuous approaches: they represent a tumor as a saturated medium, which comprises at least a solid cell phase and a liquid phase, with possible generalization to a multiplicity of other phases [12,20,23,44,52–56]. The system is then set to evolve following mass and momentum balance equations, that are closed with appropriate constitutive laws [46,57–60]. Growth of malignant aggregates is also described by continuous methods based on the so-called *adaptive dynamics*. As reviewed in [61], these models are built on the idea that the evolution of a heterogeneous element is mainly driven by selection and mutation. The former favors the diffusion of cell variants with the most adapt phenotype, whereas the latter allows the emergence of offsprings with slightly different determinants with respect to their progenitors. Differentiation across malignant masses and selection of cell clones with evolutionary advantage are finally included in continuous models based on information [62] and on game [63] theory.

On the opposite, discrete models, widely known as Individual-based models (IBMs) or Cellular Automata (CA), approach the biological problem with a microscopic point of view: they in fact represent biological entities, e.g., malignant cells or ECM components, as one or more spatial units. There are two main types of discrete models: lattice-free and lattice-based. The former one allows biological agents to have an arbitrary morphology and to freely move in space. In the latter one, the morphology of the elements and their possible movements are instead restricted according to the discretization of the spatial domain, which can be either regular (as in the case of square or cubic grids) or irregular (Voronoi tessellations). In most discrete models, malignant cells then behave according to Newtonian laws or to sets of prescribed phenomenological rules, which they execute depending on their type and on the signals received from the neighbors and/or from the environment [64–69]. Cell dynamics can be also established by an iterative minimization of the free energy of the system [70–73]. Discrete models for tumor growth can also include vascular elements, that are typically represented as line segments, interconnected lattice patterns, or collections of individual endothelial cells. In this respect, it is substantially easy to model mechanisms such as vessel sprout, branching, and anastomosis, endothelial cell activation, proliferation, and migration up to gradients of tumor angiogenic factors [37,42,74–79].

Every method has however its advantages and disadvantages. In particular, continuous techniques overlook the behavior of single cells and also fail to describe their mutual interactions. They may therefore be unsatisfactory since what occurs at the cell-scale is, as seen, fundamental in determining the invasiveness and the metastatic potential of a cancer. On the other hand, discrete models do not usually describe subcellular processes, and thus neglect molecular and genetic mechanisms that underly the evolution of the disease. Furthermore, they are difficult to be analytically studied and the associated computational cost rapidly increases with size of the system.

The use of *hybrid* modeling environments, that integrate both types of approaches, is indeed increasing over years: the aim is to create computational frameworks able to span a wide range of spatio-temporal scales with a sufficient level of accuracy, offering the advantages brought by the different methods. In a first family of hybrid methods, the same cell-scale elements are described by spatially extended (i.e., discrete) objects in selected portions of the domain and by density/concentration fields in other regions. The cross-talk between the different subdomains is defined by suitable mathematic procedures, such as hydrodynamic limits and homogeneous and/or coarse-graining methods. For example, in [21,80], an agent-based approach is used to model the outer proliferating rim of an avascular tumor whereas a continuum description is employed for the inner region of the mass, mainly formed by quiescent and necrotic tissue. The two different types of mathematical descriptions are simultaneously used also in [81]: in particular, the interactions between the discrete fraction of the lesion and its continuous part are incorporated in mass and momentum conservation laws.

The most common family of hybrid models, and historically the first, instead uses discrete variables to reproduce cell-scale elements and continuous fields to represent molecular elements. The two component parts of system then affect one each other by exchanging information. For instance, duplication/death processes of finite-size tumor cells are typically related to the diffusion of environmental nutrients [70,72,82], genetic dynamics [83,84], or presence/amount of specific control molecules [85]. Determinants of cell automata, such ad adhesion and motility, are set to depend on chemical kinetics as well [74,86]. On the other hand, continuous equations of molecular variables can have sink and source terms closely related to the actual configuration of spatially-extended malignant agents [72,73,87–92].

Motivation of the work We here introduce a multiscale approach that belongs to the previously-defined second family of hybrid models. It is used to study the avascular growth of a generic solid tumor with a heterogeneous nature, i.e., formed by cells characterized by different metabolic states. We represent malignant cells as non-deformable physical objects with finite size. They can undergo proliferation, apoptosis, necrosis, and vary their metabolic state according to stochastic and deterministic laws, that include a simplified description of the cell cycle. The evolution of the tumor mass is then shaped by its interaction with the surrounding molecular landscape, that is represented in terms of continuous variables. In particular, we account for (i) the oxygen supplied by the preexisting vasculature, whose kinetics are described by a parabolic PDE, (ii) the structural extracellular matrix (ECM), whose local density is measured by a field variable that, for the sake of simplicity, neglects its fibrous component, and (iii) tumor-secreted matrix-degrading enzymes (MDEs), whose concentration is set to vary according to a reaction–diffusion equation (RDE).

As a relevant feature of our model, malignant agents are set to move in order to *maximize a local score*, which is a sort of measure of the attractiveness of their possible target locations and is based on the trade-off between their adhesiveness (i.e., their epithelial trait) and their tendency to move towards zones of higher oxygen availability (i.e., their mesenchymal trait). The possibility of effective cell displacement is further biased by the local structure of the ECM and by the related capacity of the tumor to release proteolytic enzymes.

The progression of the malignant node is then numerically assessed, in terms of invasive depth, morphology, and internal composition, upon variations in cell biophysical determinants (i.e., adhesiveness, mitotic rate, MDE production) and environmental conditions (i.e., tissue oxygenation, ECM spatial configuration), in a close comparison with empirical evidence and observations.

The proposed model has its own characteristics and novelties:

- The rule underlying cell movement is substantially different w.r.t. those employed in most similar models, where cells are typically set to move in order to *minimize a global energy* and not to maximize a local score (see the above literature overview, and in particular the Refs. [70,71] and those relative to the Cellular Potts Model [72,73,93,94]);
- Metabolic state transitions simultaneously depend on intracellular clocks, environmental conditions, and stochastic aspects, being also characterized by a limited number of parameters, each with an immediate biological meaning. As far as we know, this level of details is not present in most hybrid approaches, where variations in cell states are typically established either by intracellular chemical profiles *or* by intracellular clocks, as the Reader can ascertain in the excellent reviews [3,66,74,95–105].

Outline of the paper The rest of the paper is organized at it follows: in Section 2, we will present the proposed model with the underlying assumptions. Section 3 will deal with its numerical implementation. In particular, we will first give details on the parameters estimate and on the indices that will be used to quantify tumor progression. We will then turn to describe the growth of the malignancy in a number of selected settings, with a close comparison with proper experimental evidence. The article will end in Section 4 with a review of the model results from a therapeutic perspective and a discussion on its limitations, with hints for possible developments.

2. Mathematical model

We use a two-dimensional lattice $\Omega \subset \mathbb{R}^2$ to reproduce a planar cross-section of a tissue with a nascent malignancy. The domain Ω is formed by identical hexagonal mesh elements: each of them is uniquely identified by its center $\mathbf{x} \in \mathbb{R}^2$ and, for any time $t \in T = [0, t_\mathrm{f}] \subset R_0^+$ (being t_f the final observation instant), labeled by an integer number $\sigma(\mathbf{x}, t) \in \mathbb{N}$, see Fig. 1 (A) and Table 1. The quantity σ can be interpreted as a sort of *spin value*: as clarified in the following, it allows to specify if the corresponding lattice element is occupied by the lesion or if it is a part of the extratumoral space. A first neighbor of a given mesh site $\mathbf{x}$ is denoted by $\mathbf{x}'$, while its overall first neighborhood by $B_\mathbf{x}$, i.e., $B_\mathbf{x} = \{\mathbf{x}' \in \Omega : \mathbf{x}' \text{ is a first neighbor of } \mathbf{x}\}$, see again Fig. 1 (A).

Tumor cells are here assumed to be finite-size non-deformable elements: each of them is set to occupy an entire grid site and assigned[1] an identification number $i \in \{1, \dots, N(t)\}$, $N(t)$ being their amount at time t. If the generic ith cell occupies at a given time $t \in T$ the mesh element $\mathbf{x} \in \Omega$, we set $\sigma(\mathbf{x}, t) = i$, see Fig. 1 (B). As shown in the same image, all mesh sites not occupied by the malignancy are labeled by the spin $\sigma = 0$: they are hereafter denoted with the adjectives "free" and "empty" and set to constitute an undifferentiated extratumoral environment. In other words, a grid site of the domain has spin value equal to 0 if it is not occupied by a tumor agent; otherwise, it is assigned a spin value equal to the identification number of the malignant cell by which it is actually occupied. Obviously, the total amount of malignant agents cannot exceed the overall number of domain grid elements.

Each tumor cell is then given a metabolic state, that falls within the set:

$$\mathcal{P} = \{\text{“D” (default), “M” (mitotic), “A” (apoptotic), “H” (hypoxic), “N” (necrotic)}\}.$$

In this respect, $p(i, t) \in \mathcal{P}$ indicates the state of the ith malignant agent at the time instant $t \in T$, see Table 1. We also account for the possibility of state transitions: as specified in the following, they are considered almost instantaneous processes and governed by either stochastic or deterministic laws.

The field variables $o(\mathbf{x}, t), m(\mathbf{x}, t) : \Omega \times T \to \mathbb{R}_0^+$ are instead used to define the concentrations of oxygen and of tumor-secreted matrix-degrading enzymes (MDEs), respectively, see Table 1. The function $e(\mathbf{x}, t) : \Omega \times T \to [0, 1]$ finally gives a normalized and non-dimensional measure of the local density of the extracellular matrix (ECM). It is used to describe the heterogeneity characteristic of *in vivo* matrices, that range from loose areas, composed of sparse proteins, to highly dense regions, composed of an overabundance of collagenous elements [106,107]. For the sake of simplicity, we neglect the fibrous component of the ECM, despite it plays a key role in cell migration, specially in three-dimensional settings [108–112].

2.1. Molecular dynamics

The above-defined chemical variables are set to evolve according to classical partial differential equations. In particular, oxygen is assumed to freely diffuse within the tissue and be uptaken by viable tumor cells as a part of their metabolism. The evolution of its concentration, o, can be indeed described as follows:

$$\frac{\partial o}{\partial t}(\mathbf{x}, t) = \underbrace{D_\mathrm{o} \nabla^2 o(\mathbf{x}, t)}_{\text{diffusion}} \underbrace{- \mu_\mathrm{o} o(\mathbf{x}, t) \mathbb{1}(\sigma(\mathbf{x}, t) = i : p(i, t) \in \{\text{D,H,M}\})}_{\text{cell uptake}} \underbrace{- \lambda_\mathrm{o} o(\mathbf{x}, t)}_{\text{decay}}. \tag{1}$$

In Eq. (1), the coefficient μ_o is a measure of the absorption of the chemical by metabolically-active malignant agents (i.e., $\mathbb{1}$ is the indicator function), whereas the rate λ_o measures its natural decay. The constant coefficient D_o implies a homogeneous and isotropic diffusivity: it is a reasonable approximation, although oxygen has to pass through cell membranes and interstitial fluids of different compositions [113,114]. The spatial distribution of the chemical nutrient may be also given by a partial pressure field, that can be quantified by normalizing its concentration with a proper solubility coefficient.

The ECM density, represented by the normalized field e, is set to be locally reduced by the activity of tumor-produced proteolytic enzymes, whose concentration is given by the variable m. This leads to the following coupled equations:

$$\frac{\partial e}{\partial t}(\mathbf{x}, t) = \underbrace{- \mu_\mathrm{e} e(\mathbf{x}, t) m(\mathbf{x}, t)}_{\text{ECM degradation}}; \tag{2a}$$

$$\frac{\partial m}{\partial t}(\mathbf{x}, t) = \underbrace{D_\mathrm{m} \nabla^2 m(\mathbf{x}, t)}_{\text{diffusion}} \underbrace{+ \mu_\mathrm{m} \mathbb{1}(\sigma(\mathbf{x}, t) = i : p(i, t) \in \{\text{D,H,M}\})}_{\text{cell production}} \underbrace{- \lambda_\mathrm{m} m(\mathbf{x}, t)}_{\text{decay}}, \tag{2b}$$

where μ_e is the rate of matrix degradation, D_m is the (substantially low) diffusion constant of MDEs, while μ_m and λ_m are their production and decay rate, respectively. Eqs. (2a)–(2b) imply that the malignant mass is able to locally reduce the density of the surrounding matrix: this possibly increases the ability of tumor cells to push into the host tissue by creating optimal space for infiltration (cf. Section 2.3).

The initial profiles of the molecular substances included in our model will be specified later on, as the boundary conditions integrating Eqs. (1) and (2b). From a mathematical perspective, the field variables o, e, m are continuous in time and piecewise continuously differentiable in space (i.e., $o, e, m \in PC^1(\Omega, T)$). Their positivity is then preserved over time by the Eqs. (1), (2a), and (2b), i.e.,

$$o(\mathbf{x}, 0), e(\mathbf{x}, 0), m(\mathbf{x}, 0) \geq 0, \quad \forall\, \mathbf{x} \in \Omega \Longrightarrow o(\mathbf{x}, t), e(\mathbf{x}, t), m(\mathbf{x}, t) \geq 0, \quad \forall\, (\mathbf{x}, t) \in \Omega \times T.$$

The estimate of the parameters introduced in the above equations is given in Section 3.1 and collected in Table 2.

---

[1] Each tumor cell initially present within the domain is assigned a random identification number $i \in \{1, \dots, N(0)\}$. Updates in the set of cell identification numbers are then determined by metabolic state transitions, as established by the corresponding rules explained in Section 2.2.

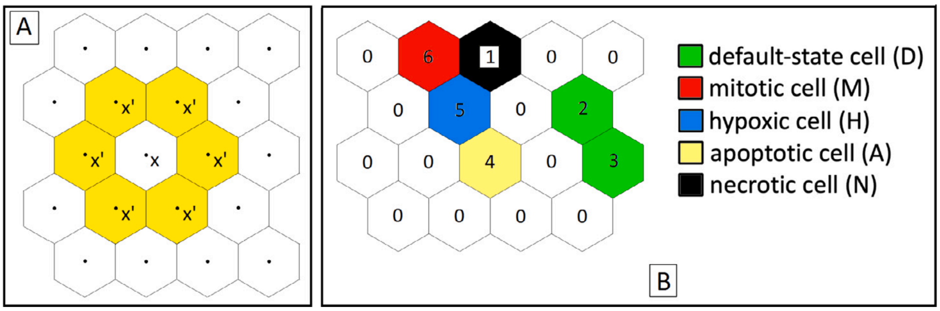

Fig. 1. (A) Representative region of the domain Ω with a given grid element $\mathbf{x}$ and its first neighborhood $B_{\mathbf{x}}$. (B) Subdomain including 6 malignant cells with different metabolic states (labeled by the set of identification numbers $\{1,\dots,6\}$), surrounded by extratumoral tissue (composed of the free grid elements identified by the spin value $\sigma = 0$).

Table 1
Summary of variables and acronyms introduced in the model.

Variable/Acronym	Description
t	time
$\mathbf{x}$	center of a grid site
$\sigma \in \mathbb{N}$	grid site spin value
$i \in \{1,\dots,N(t)\}$	cell identification number
"D"	cell default state
"M"	cell mitotic state
"A"	cell apoptotic state
"H"	cell hypoxic state
"N"	cell necrotic state
$o(\mathbf{x},t)$	oxygen concentration
$m(\mathbf{x},t)$	MDE concentration
$e(\mathbf{x},t)$	normalized ECM density

2.2. Cell state transitions

Tumor cells are allowed to instantaneously vary their metabolic state according to either stochastic or deterministic laws, that are set to depend on intracellular clocks and environmental stimuli, as sketched in Fig. 2 (A).

Malignant agents in normoxic conditions are given the default state "D": they can then become hypoxic, duplicate, or undergo apoptosis. In particular, a default-state cell i becomes hypoxic at a given time $t \in T$ when the available oxygen level locally drops below a basal threshold, i.e., if $o(i,t) \le o_{\mathrm{H}}$, where $o(i,t)$ indicates the chemical concentration at the mesh element actually occupied by the agent of interest (i.e, the exact formal notation would be $o(\mathbf{x} : \sigma(\mathbf{x},t) = i, t)$). On the opposite, a hypoxic cell i returns to the default state at $t \in T$ if $o(i,t) > o_{\mathrm{H}}$, i.e., if normoxia is locally restored.

A default-state malignant agent i enters the mitotic state "M" at a given time $t \in T$ with a probability that depends on a sort of internal clock:

$$\Pr(p(i,t) : \mathrm{D} \to \mathrm{M}) = -\frac{\alpha_{\mathrm{DM}}}{t_{\mathrm{M}}^2}(t - t_i)\left[(t - t_i) - 2t_{\mathrm{M}}\right]. \tag{3}$$

In the above law, plotted in Fig. 2 (B-left graph), t_i identifies the time instant at which the cell of interest was born/underwent the last duplication (it is set equal to 0 for the group of agents forming the original node of the disease), whereas t_{M} indicates an average duration of the mitotic cycle. The coefficient $\alpha_{\mathrm{DM}} \le 1$ finally gives the maximal probability of proliferation: it is here considered constant, despite it in principle depends on cell determinants (e.g., genetic profile) and microenvironmental variables (e.g., availability of nutrients such as glucose). Eq. (3) indeed states that the duplication probability of a cell in a default state increases, starting from its birth/last mitosis, until a maximum and then decreases to become negligible.

As shown in Fig. 2 (C), the mitotic process is implemented by creating a new agent in a *free* grid site within the neighborhood of the duplicating cell. In mathematical terms, if the progenitor cell i is currently in the mesh element $\mathbf{x} \in \Omega$ (i.e., if $\sigma(\mathbf{x},t) = i$), the daughter agent is created in one of the free sites $\mathbf{x}' \in B_{\mathbf{x}}$, selected at random. If the surrounding mesh elements are full of cells, the duplication process does not indeed occur. This is the model counterpart of the mechanism of *contact inhibition of proliferation*, i.e., the mitotic cycle is typically disrupted in overcompressed cells, although abnormal proliferation is a relevant characteristic of malignant masses (cf. [115] and references therein). The new born agent is then given the lowest identification number among those actually free, that also include the values previously referred to apoptotic cells (see below and panel (C) of Fig. 2). Temporarily, the daughter agent is assigned the mitotic state "M": however, at the subsequent iteration of the algorithm, it will automatically acquire the default state "D", which will be also given to its progenitor.

Hypoxic and default-state cells can undergo apoptosis, which is a programmed death mainly regulated by intracellular clocks and related signaling pathways. More specifically, at any given $t \in T$, a cell i with phenotype "D" or "H" is set to die (i.e., to acquire an apoptotic state) with the following Hill-type probability, which is reproduced in Fig. 2 (B-left graph):

$$\Pr(p(i,t) : \{\mathrm{D},\, \mathrm{H}\} \to \mathrm{A}) = \frac{(t - t_i)^4}{(t - t_i)^4 + t_{\mathrm{M}}^4}, \tag{4}$$

where t_i and t_{M} are defined as in the previous Eq. (3). Apoptotic cells are deleted from the simulation domain to model the natural decay of their body: they indeed free both space, which is added to the extratumoral region, and identification numbers, which become available for newborn agents, see Fig. 2 (C).

A hypoxic cell i is here assumed to undergo necrosis according to a probability with a Michaelis–Menten form if the local level of oxygen has a further drop below the critical threshold o_{N}:

$$\Pr(p(i,t) : \mathrm{H} \to \mathrm{N}) = \frac{(t - t_i^{\mathrm{H}})}{(t - t_i^{\mathrm{H}}) + 0.5t_{\mathrm{N}}} H(o_{\mathrm{N}} - o(i,t)), \tag{5}$$

In the above equation, reproduced in Fig. 2 (B-right plot), H indicates the Heaviside function (i.e., $H(z) = \{1, \text{ if } z \ge 0; 0, \text{ if } z < 0\}$), t_i^{H} identifies the instant at which the cell of interest lost its normoxic state, and t_{N} is an average time lapse during which tumor agents can remain deprived of oxygen before a complete disruption of their metabolic activity. Necrotic cells are not removed from the simulation environment: they maintain their identification number and remain frozen in their last position, thereby affecting the possibility of movement and proliferation of viable agents, see Fig. 2 (C). Metabolically death cells are in fact observed to have full rigidity and incompressibility since their solid volume fraction is replaced by calcium phosphate and/or calcium oxalate molecules, that bind together and form calcite crystals.

Eqs. (3), (4), and (5) have to be intended as the probabilities that a given cell i undergoes the corresponding state switch in the interval

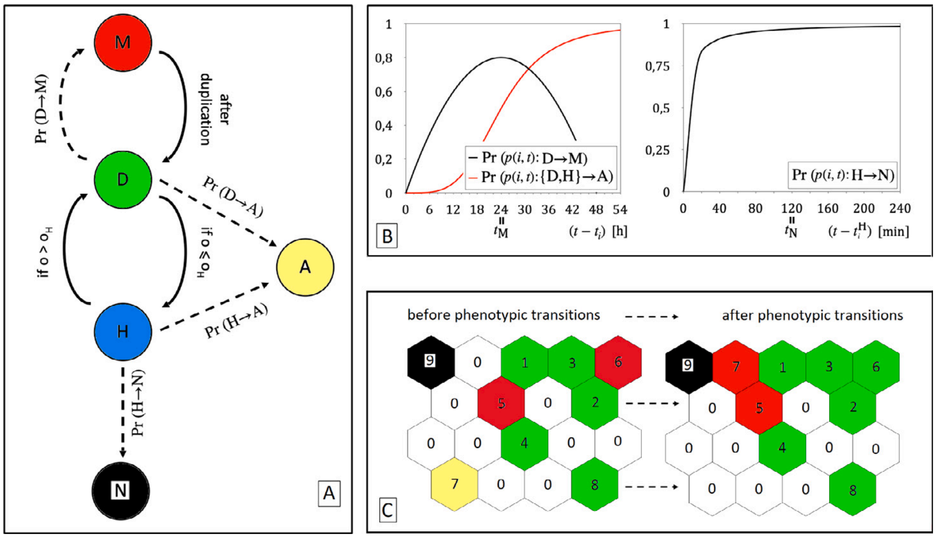

Fig. 2. (A) Cell metabolic states included in the modeling framework and relative transitions. Dashed arrows indicate stochastic variations, whereas full arrows are used for deterministic switches. (B-left plot) Probabilistic laws determining cell mitotic/apoptotic events (cf. Eqs. (3) and (4)). (B-right plot) Probabilistic law underlying the necrotic transition of a cell i subjected to oxygen deprivation, i.e., such that $o_N \geq o(i,t)$ (cf. Eq. (5)). (C) Examples of cell state transitions and update in the set of identification numbers: the apoptotic cell 7 is removed from the domain, whereas the necrotic agent 9 remains frozen within the tissue. The cells 5 and 6 are both in a mitotic condition. However, only the former one has empty space within its first neighborhood to proliferate. As a consequence of its duplication, a new cell is added to the domain, which is assigned the identification number 7 of the apoptotic agent and the mitotic state "M". At the next time step, both the parent and the daughter cells will acquire the default state "D".

$(t-\Delta t, t] \subset T$, Δt being the discretization step of T. They are indeed the discrete counterparts of stochastic laws that have in principle to be defined on temporal continuous domains. The values of the parameters included in Eqs. (3), (4), and (5) are finally given in Section 3.1 and summarized in Table 2.

2.3. Cell movement

Tumor cells are here set to move in order to maximize a non-dimensional and normalized *local score*, defined by a function $\mathcal{S}(\mathbf{x},t) : \Omega \times T \longrightarrow [0,1]$. In particular, for any mesh element $\mathbf{x} \in \Omega$ and time $t \in T$, $\mathcal{S}$ is determined by a *trade-off* between intercellular adhesion and individual tendency to migrate towards tissue areas rich of oxygen, with a *bias* given by the local structure of the ECM:

$$\mathcal{S}(\mathbf{x},t) = \underbrace{-4e(\mathbf{x},t)(e(\mathbf{x},t)-1)}_{\text{ECM effect}} \underbrace{\left(s_1 \frac{\#C_{\mathbf{x}}(t)}{6} + s_2 \frac{o(\mathbf{x},t)}{\max_{\mathbf{y}\in\Omega} o(\mathbf{y},t)}\right)}_{\text{adhesion vs. chemotaxis}} \in [0,1], \quad (6)$$

where, as previously seen, e is the normalized density of extracellular matrix and o measures the oxygen concentration. In Eq. (6), the symbol }}#″ indicates the cardinality of the set

$$C_{\mathbf{x}}(t) = \{\mathbf{x}' \in B_{\mathbf{x}} : \mathbf{x}' \text{ is occupied by a cell at time } t\}, \quad (7)$$

whereas 6 is the maximal possible number of neighbors per agent, cf. Fig. 1 (A). We then set

$$\begin{cases} s_1, s_2 \in [0,1]; \\ s_1 + s_2 = 1. \end{cases} \quad (8)$$

The two coefficients can be indeed interpreted as weights that establish the relative preference of malignant cells for clusterization (s_1) or for crawling up to chemical gradients (s_2). In other words, they are a quantification of the cell expression of epithelial (s_1) or mesenchymal (s_2) traits.

The parabolic relationship between ECM density and cell movement capacity in Eq. (6) is consistent with a wide range of experimental observations. For instance, in both two- and three-dimensional settings, very sparse matrices, constituted by a substantially low amount of fibers/ligands, give rise to poor cell displacement. This is due to the fact that migrating agents are unable to find sufficient collagen-like sites to attach and use for traction and forward locomotion [116,117]. Intermediate ECM densities instead result in optimal attachment-detachment cycles of cell–matrix focal adhesions, that permit maximal cell movement [118–121]. Finally, an overabundance of matrix components dramatically prevents cell locomotion. On one hand, it in fact reduces the available space for cell body translocation; on the other hand, integrin receptors engage into too stable focal adhesions, that inhibit efficient cell movement [122,123].

Cell spatial dynamics are then implemented by the following procedure. At any simulation time $t \in T$, we calculate for each cell i in the hypoxic or in the default state (i.e., for each agent i such that $p(i,t) \in \{\text{H}, \text{D}\}$), the score $\mathcal{S}$ both of its actual location $\mathbf{x}_s \in \Omega : \sigma(\mathbf{x}_s, t) = i$ ("s" for source) and of the *free* grid elements belonging to the neighboring region $B_{\mathbf{x}_s}$. The cell of interest then chooses its possible target destination $\mathbf{x}_t$ according to the following law:

$$\mathbf{x}_t = \underset{\substack{\{\mathbf{y}\in B_{\mathbf{x}_s}\} \cup \{\mathbf{x}_s\} \\ \mathbf{y} \text{ is free}}}{\arg\max} \; \mathcal{S}(\mathbf{y},t). \quad (9)$$

A malignant cell may indeed move or even stay still, i.e., if the maximal score $\mathcal{S}$ is associated to its actual position (in this case $\mathbf{x}_t \equiv \mathbf{x}_s$), see Fig. 3. In the case of effective cell displacement, $\mathbf{x}_s$ is immediately assigned to the extratumoral space, i.e., $\sigma(\mathbf{x}_s)$ is set equal to 0. If the local score is maximized in a multiplicity of grid sites in the subdomain of interest, the malignant agent is assumed to opt for one of them selected at random.

We prohibit movement of cells in a mitotic state in accordance with the well-known "Go-or-Grow" (GoG) hypothesis. It in fact states that proliferation and migration are two mutually excluding processes and that there is in general an inverse correlation between cell migratory potential and duplication rate. The GoG paradigm is built on experimental observations relative to a wide spectrum of malignancies, see [124,125] and references therein, and successfully employed in the theoretical literature [126–129]. Hypoxic cells are instead allowed to move but inhibited to duplicate, see Section 2.2: high levels of hypoxia-inducible factors, such as HIF-1, are in fact demonstrated to result in the overexpression of genes relative to the migratory machinery and in the underexpression of genes related to the mitotic cycle, see [130,131].

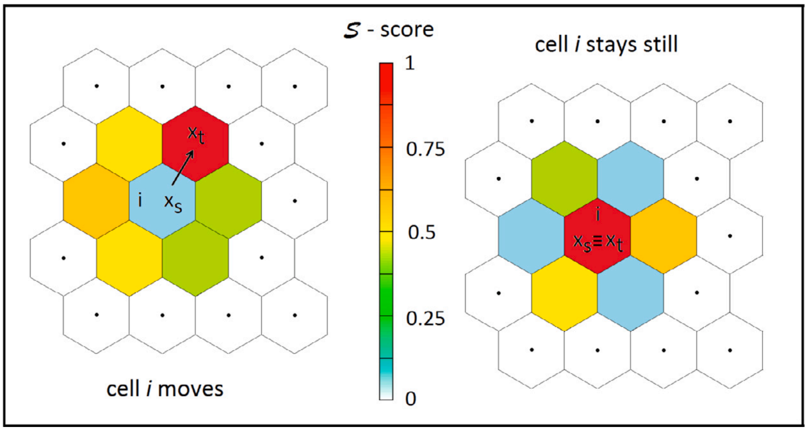

Fig. 3. Implementation of cell movement. A cell i (either in the default or in the hypoxic state) occupies a grid element $\mathbf{x}_s$. The local score $\mathcal{S} \in [0,1]$ is then evaluated both for $\mathbf{x}_s$ and for the free neighboring mesh elements. The cell i is finally set to move (left scenario) or stay still (right scenario) in order to take place in the grid element (among those taken into account) characterized by the maximal value of $\mathcal{S}$.

3. Model simulation and results

3.1. Simulation details

We employ a quasi-rectangular simulation domain Ω formed by $1.339 \cdot 10^3$ hexagonal grid elements, whose apothem is set to measure 10 μm, see Fig. 5. Ω indeed represents a planar section of a tissue with an extension of ≈ 0.5 mm^2, whereas our *in silico* malignant agents have an area of ≈ 350 μm^2, which is consistent with the mean dimension of tumor cells organized in spheroid aggregates [132–134]. We use a uniform discretization for the time domain T, with step equal to $\Delta t = 1$ min. All forthcoming simulations are then run until $t_f = 60$ days: the considered time lapse is sufficiently large to capture a significant evolution of the malignant mass but low enough to allow us to neglect extratissutal dynamics (such as tumor infiltration in the vascular network), that are beyond the scope of this study.

The proposed model is implemented by an algorithm that consists first in the initialization of the system and then in iterations of the following 3 steps, see Fig. 4:

1. Default and hypoxic cells currently present within the domain move (or stay still) according to the rule introduced in Eq. (9);
2. State transitions, as long as events of apoptosis and proliferation, are implemented in this sequence:
   - Deterministic default-to-hypoxic switches (and *vice versa*) are performed;
   - The resulting population of cells in the default state is checked for apoptosis;
   - The resulting population of hypoxic cells is checked first for necrosis and then for natural death;
   - The resulting population of default-state cells is checked for mitosis, with duplication events implemented as described in Section 2.2.

   At any algorithmic step, the malignant cells belonging to a given subgroup are considered one-by-one (with a randomized order), as the behavior of an agent may affect the evolution of the others. For example, a default-state cell subjected to apoptosis is removed from the tissue thereby freeing space (and identification number) for its viable groupmates to move or duplicate. The numerical steps 1) and 2), that establish cell-level dynamics, are based on the chemical profiles obtained in the previous iteration.
3. The kinetics laws for the molecular variables, i.e., Eqs. (1), (2a), and (2b), are rederived accounting for the cell configuration resulting from the above steps 1) and 2) and solved by a time-explicit Euler method coupled with a Galerkin finite-element technique, which is employed on the hexagonal mesh underlying the spatial domain Ω.

The proposed algorithm is coded in a C++ language, with Visual Studio 2019 as IDE, whereas the resulting simulations are run on a PC with Intel(R) Core(TM) i5-5200U CPU (2.20 GHz-8 GB RAM) and the Windows 7 64-bit operating system.

Initial system configuration. All forthcoming realizations start with a node of 7 malignant cells in a default-state (“D”), placed in the bottom area of the domain Ω, see Fig. 5 (top panel). This configuration reproduces the progenitor bulk of a tumor mass, which has established a foothold in the basement membrane of the host tissue and has the potential for further expansion.

A basal concentration of oxygen is homogeneously distributed across the entire domain: in particular, the initial amount of the chemical is larger than the hypoxic threshold to simulate a tissue still not compromised by the lesion. We then set an initial ECM density which is spatially uniform and high enough to prevent early migration of malignant cells. Finally, there are no MDEs at the beginning of the simulations. Summing up, Eqs. (1), (2a), and (2b) are completed with the following initial conditions:

$$o(\mathbf{x},0) = o^{\mathrm{in}} = 4 \cdot o_{\mathrm{H}}; \qquad e(\mathbf{x},0) = e^{\mathrm{in}} = 1; \qquad m(\mathbf{x},0) = m^{\mathrm{in}} = 0, \quad \text{for any } \mathbf{x} \in \Omega, \tag{10}$$

see the bottom panels in Fig. 5.

Eq. (1) is integrated with Dirichlet boundary conditions along the upper and the side domain edges, respectively denoted as $\partial\Omega^{\mathrm{upper}}$ and $\partial\Omega^{\mathrm{side}}$, to mimic oxygen supply from the preexisting normal vasculature at a constant rate $o^{\mathrm{b}} = 2.8 \cdot 10^{-15}$ μM/μm^2, as done in [135]. No flux (Neumann) boundary conditions are instead set for the oxygen on the bottom edge of the domain ($\partial\Omega^{\mathrm{bottom}}$) and for the malignant MDEs on the entire domain boundary ($\partial\Omega$). In mathematical formulation, we indeed have

$$\begin{cases} o(\mathbf{x},t) = o^{\mathrm{b}}, & \text{if } \mathbf{x} \in \partial\Omega^{\mathrm{upper}} \cup \partial\Omega^{\mathrm{side}}; \\ \nabla o(\mathbf{x},t) = 0, & \text{if } \mathbf{x} \in \partial\Omega^{\mathrm{bottom}}; \\ \nabla m(\mathbf{x},t) = 0, & \text{if } \mathbf{x} \in \partial\Omega, \end{cases} \tag{11}$$

for any $t \in T$.

Variations in the initial and/or boundary conditions will be explicitly mentioned in the forthcoming sections.

Parameter estimate. The chemical kinetics included in our approach are based on parameters widely measured in empirical models (with little discrepancy across the different experimental settings). In particular, the diffusion coefficient of oxygen, D_o, is here fixed to $3.6 \cdot 10^6$ μm^2/h, as reported in [4,128], whereas its decay rate, λ_o, to $3.6 \cdot 10^{-4}$

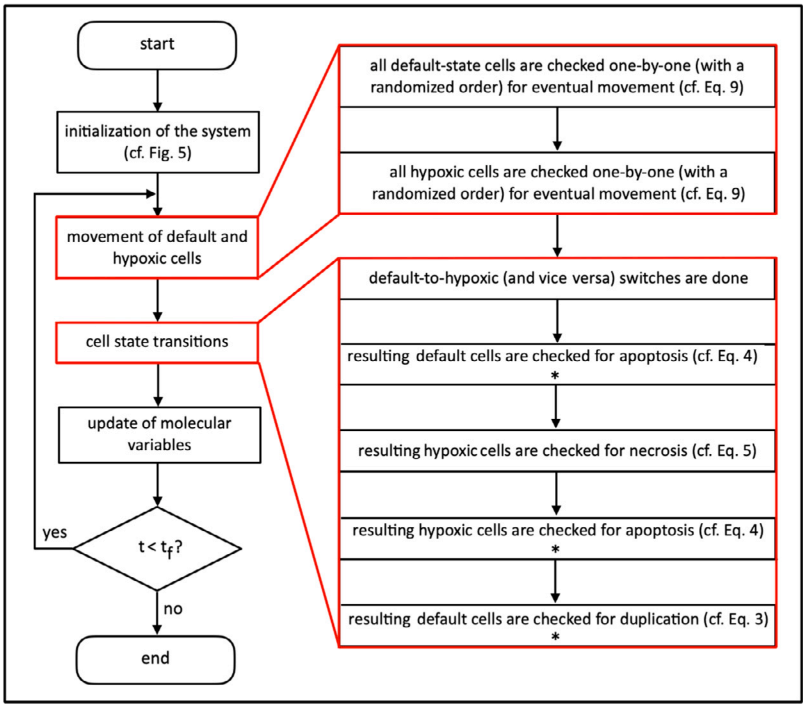

Fig. 4. Schematic flowchart of the algorithm developed to simulate the proposed model. The asterisks (" * ") indicate the numerical steps that need an update in the cell identification numbers, as explained in Section 2.2.

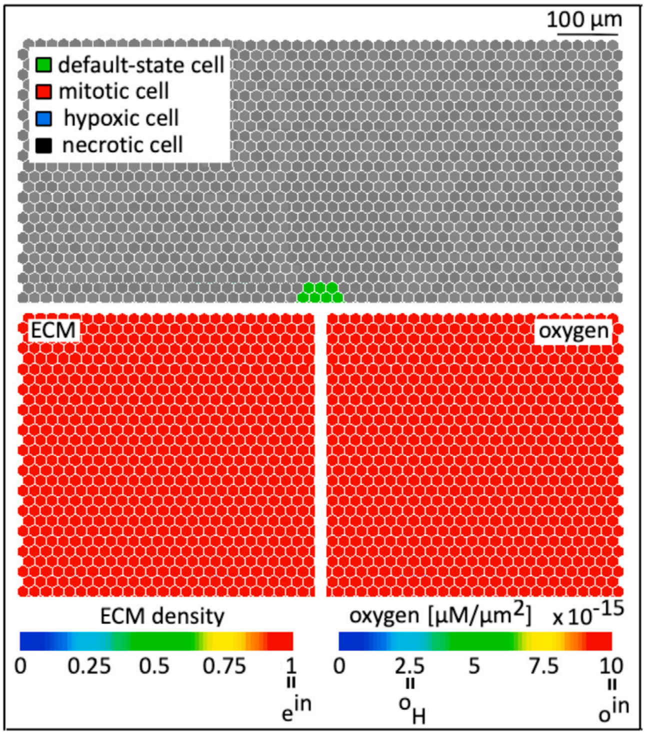

Fig. 5. Initial configuration of the system. The progenitor tumor consists of a node of 7 cells in the default state, whereas the host tissue is initially characterized by an overdense ECM (left semi-domain) and by a sufficient oxygenation (right semi-domain), cf. Eq. (10).

h^{-1}, in accordance with [136]. The effective oxygen (rsp., matrix) consumption rate, given by the parameter μ_o (rsp., μ_e), is set equal to $1.67\cdot 10^{-10}$ h^{-1} (rsp., $0.5\cdot 10^{-8}$ μm^{2}h^{-1} μM^{-1}), taking advantage of the experimental observations in [9,137,138]. A low $D_m = 4.4\cdot 10^{-4}$ μm^{2}h^{-1} is fixed since matrix-degrading enzymes are observed to poorly spread away from cell membranes [107,139], with the implication of a strongly localized ECM degradation. Production and decay of the tumor-secreted proteolytic enzymes are finally quantified by $\mu_m = 1.38\cdot 10^{-6}$ h^{-1} and $\lambda_m = 0.55\cdot 10^{-6}$ h^{-1}, in agreement with [107]. The values of the coefficients μ_o and μ_m are here assumed to be equal for all cells with an active metabolism: further specifications are avoided in the absence of experimental measures able to clearly establish how these two quantities vary during the cell cycle or upon changes in the intracellular level of oxygen (i.e., if it remains above the necrotic threshold).

The coefficients regulating cell state transitions are taken from the experimental literature relative to brain tumors: this choice is done to have a coherent parameter setting, although we deal with a generic malignancy[2]. In particular, we first assume that the average duration of the cell cycle, indicated by t_M, is 24 h [140]. The oxygen level that leads to hypoxia, o_H, is then set equal to $2.5\cdot 10^{-15}$ μM/μm^2, in agreement with the values used in [128,141] in the case of glioblastomas.

The necrotic threshold is fixed to $o_N = o_H/4$, whereas the Michaelis–Menten coefficient t_N, that quantifies the average survival time of a cell subjected to an almost complete oxygen deprivation, to 2 h. Their simultaneous estimate is obtained by preliminary simulations run to fit the time needed by a virtual tumor agent to undergo necrosis starting from normoxic conditions (i.e., from a level of oxygen equal to $o^{in} = 4\cdot o_H$), in the case of chemical consumption without supply, with the corresponding experimental value, quantified to 16 h in [140] for selected glioma cell lines, see Fig. 6 (A).

As shown in Fig. 6 (B), the coefficient α_{DM}, introduced in Eq. (3), is finally fixed to 0.8. This results in a mitotic rate of artificial tumor cells (defined as the number of agents that duplicate in a given time

---

[2] Our approach does not aim to strictly reproduce growth and invasion of gliomas or glioblastomas. We in fact do not include critical aspects that characterize and affect the evolution of these types of disease, such as brain composition, morphology, and mechanical properties.

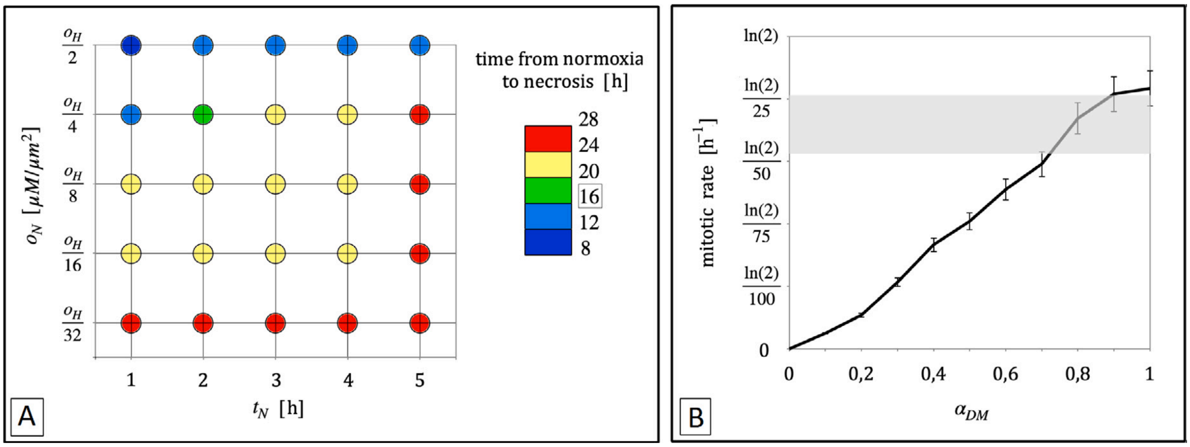

Fig. 6. Estimate of model parameters. (A) Time needed to pass from normoxia to necrosis by a representative virtual tumor cell, which is allowed to consume oxygen without an environmental supply, for different pairs (o_N, t_N). The values in the graph are averaged over 20 independent simulations; standard deviations are not explicitly represented as they are substantially small, i.e., $< 3\%$ of the corresponding mean. The experimental counterpart of this quantity is 16 h [140]. We recall that $o_H = 2.5 \cdot 10^{-15}$ μMμm^{-2} indicates the oxygen level leading to hypoxia, see Table 2. (B) Mitotic rate of our virtual tumor (given as the mean ± s.d. over 20 independent numerical realizations) in the case of different values of α_{DM}. The grey shadow in the plot indicates the range of the corresponding empirical quantity.

Table 2
Summary of the parameters employed in the model simulations.

Parameter	Description	Value [Units]	Reference(s)
t_f	final observation time	60 [days]	
Δt	time discretization step	1 [min]	
t_M	average duration of cell cycle	24 [h]	[128,142]
o_H	oxygen hypoxic threshold	$2.5 \cdot 10^{-15}$ [μMμm^{-2}]	[128,141]
o_N	oxygen necrotic threshold	$o_H/4$ [μMμm^{-2}]	
t_N	average time lapse before necrosis	2 [h]	
α_{DM}	maximal probability of duplication	0.8	[128,142]
D_o	oxygen diffusion constant	$3.6 \cdot 10^6$ [μm^2 h^{-1}]	[4,128]
λ_o	oxygen decay rate	$3.6 \cdot 10^{-4}$ [h^{-1}]	[136]
μ_o	oxygen consumption rate	$1.67 \cdot 10^{-10}$ [h^{-1}]	[9,137,138]
o^b	oxygen supply	$2.8 \cdot 10^{-15}$ [μMμm^{-2}]	[135]
D_m	MDE diffusion constant	$4.4 \cdot 10^{-4}$ [μm^{2}h^{-1}]	[107]
μ_m	MDE production rate	$1.38 \cdot 10^{-6}$ [h^{-1}]	[107]
λ_m	MDE decay rate	$0.55 \cdot 10^{-6}$ [h^{-1}]	[107]
μ_e	matrix degradation rate	$0.5 \cdot 10^{-8}$ [μm^{2}h^{-1} μM^{-1})]	[9,137,138]
o^{in}	initial oxygen concentration	$4 \cdot o_H$ [μMμm^{-2}]	
e^{in}	initial ECM density	1	
m^{in}	initial MDE concentration	0 [μMμm^{-2}]	

lapse) falling within the experimental range $[\ln(2)/48, \ln(2)/24]$ h^{-1}, as measured in the case of glioblastoma spheroids cultured *in vitro* [142].

A summary of the model parameters and of their estimate is given in Table 2, which also indicates the relative bibliographic references.

Quantification of model results. The aim of our work is to investigate how environmental conditions and cell determinants influence tumor growth. We indeed focus on the following observables, that relate both to the *macroscopic* characteristics of the disease and to its *microscopic* composition, i.e., its internal metabolic heterogeneity:

- Invasive Depth $D(t)$, which measures, for any given time $t \in T$, the radius of the half-circle that contains all malignant agents. It allows to reasonably estimate the expansion of the lesion within the host, starting with $D(0) \approx 40$ μm, as it can be evaluated in the top panel of Fig. 3;
- Necrotic Index $I_N \in [0, 1]$, which is equal to the percentage of tumor cells without metabolic activity at the end of the observation time. In this respect, $t_n \in T$ hereafter indicates the time instant at which the first necrotic cell appears within the domain Ω.

In the forthcoming sections, these quantities will be given as the mean (± the standard deviation) evaluated over 20 independent numerical realizations, in order to analyze the robustness of the simulation outcomes. Random aspects are in fact included in both cell movement and state transitions, cf. Section 2.

3.2. Variations in the trade-off between adhesion and chemotaxis

We first simulate the evolution of the malignancy in the case of perfect balance between intercellular adhesiveness and chemotaxis up to oxygen gradients, obtained by setting $s_1 = s_2 = 0.5$ in Eq. (6). As reproduced in Fig. 7 (central column of panels), a *fingering* morphology of the tumor emerges. It is the result of the following interconnected dynamics, that initiate within the first two weeks of observation:

- Groups of external cells start to degrade the surrounding matrix, therefore opening paths for invasion;
- Strands of more internal agents then follow, as a consequence both of the adhesion and of the fact that their movement is spatially biased by the proteolytic activity of their “leader” mates;

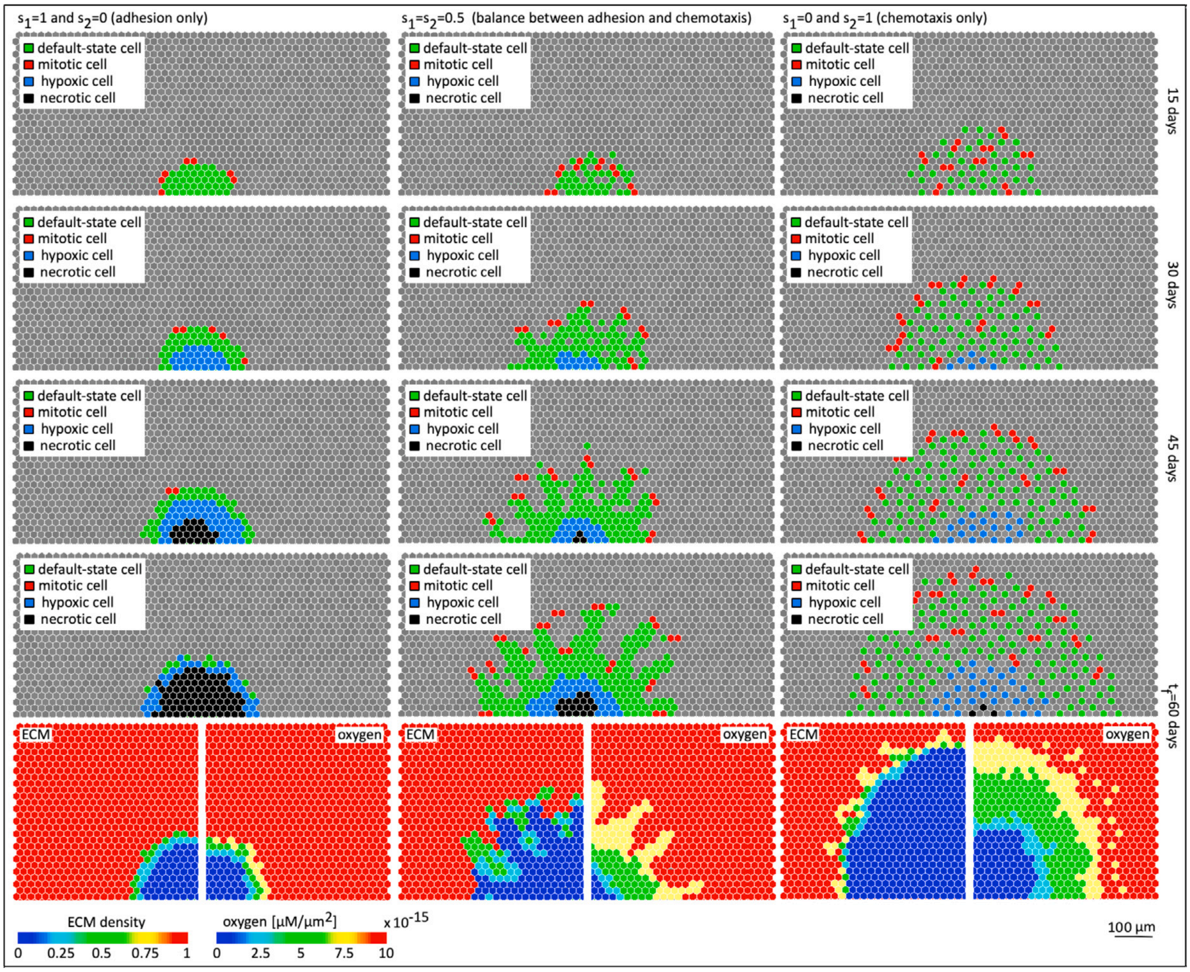

Fig. 7. Tumor growth and progression for different trade-offs between intercellular adhesiveness and cell tendency to move along oxygen gradients. In all three cases, the final patterns (i.e., at t_f = 60 days) both of the ECM density (left semi-domain) and of the oxygen concentration (right semi-domain) are shown in the bottom panels. We constantly employ the initial system configuration shown in Fig. 5, with the parameter values listed in Table 2. We also recall that the simulation setting defined by $s_1 = s_2 = 0.5$ is hereafter referred to as the *reference* one.

- Mitotic events and chemotaxis, which equally affect all malignant cells, sustain reinforcement and elongation of the protruding tumor tongues.

Hypoxic transitions start to occur at the core of the tumor after approximately a month, as the available amount of oxygen locally drops below the quantity $o_{\rm H}$. A bulk of metabolically dead cells appears at $t_{\rm n} \approx 45 \pm 4$ days; then, it enlarges simultaneously to the area of the tissue deprived of oxygen. At the end of the observation time, i.e., at $t_f = 60$ days, the malignancy presents a necrotic core (which occupies $\approx 10.2 \pm 1.1\%$ of the entire disease, see the corresponding value of $I_{\rm N}$ in Fig. 11), surrounded by a ring of hypoxic cells and by an external region of metabolically active and viable agents organized, as seen, in invasive fingers. The final invasive depth of the lesion, $D(t_f)$, is equal to 291.1 ± 27.3 μm, cf. Fig. 11.

Tumor spatial expansion is instead discouraged when cell–cell adhesion is the unique behavioral stimulus (i.e., if $s_1 = 1$ and $s_2 = 0$ in Eq. (6)). In this case, the malignant mass remains closely packed for the entire observation time: also external cells are in fact unable to detach from the core of the lesion and to spread within the tissue, see Fig. 7 (left column of panels). Hypoxia and necrosis start approximately at 30 and 45 days, respectively (in both cases the standard deviation is close to 5 days), i.e., as in the previous setting. Oxygen supply is in fact provided by diffusion from the rest of the domain, where the chemical is not significantly consumed as a consequence of the localized growth of the malignant mass. However, once appeared, the necrotic bulk rapidly extends since cancer cells have a reduced capacity to successfully escape harsh conditions due to their strong adhesive interactions. In this setting, the disease finally consists of a small and compact cluster, composed of a large portion of metabolically death tissue surrounded by a thin hypoxic region. Only few cells at the edge of the disease maintain normoxic conditions. Accordingly, we have $I_{\rm N} \approx 0.63 \pm 0.12$, $D(t_f) = 160.4 \pm 18.3$ μm, see Fig. 11.

The absence of intercellular adhesion (obtained by setting $s_2 = 1$ and $s_1 = 0$ in Eq. (6)) leads to completely different dynamics. Groups of malignant cells located at the external areas of the lesion are in fact observed to quickly loose contacts, dissociate, and spread away, creating a dispersed front, see the right panels in Fig. 7. Repulsive processes also occur within the central regions of the spheroid: a large fraction of internal cells indeed move and escape oxygen deprivation. As a consequence, necrotic phenomena are substantially delayed (i.e., $t_{\rm n} = 55.3 \pm 4.9$ days) and characterized by a poor extension (i.e., $I_{\rm N} \approx 0.02 \pm 0.005$, see Fig. 11). After two months, the host tissue is dramatically invaded by a scattered layer of malignant agents, as $D(t_f)$ is equal to 391.4 ± 31.6 μm, see the bottom-right panels in Fig. 7 and the plots in Fig. 11.

As shown in Fig. 11 (A), the tumor invasive depth grows almost linearly over the entire observation period both when cells are subjected to adhesion only and when this stimulus is coupled to chemotaxis. In

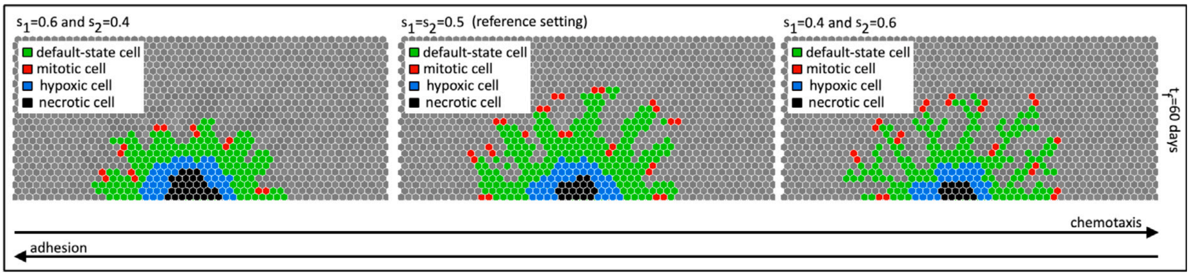

Fig. 8. Effect on tumor finger morphology of variations in the trade-off between intercellular adhesiveness and chemotaxis, i.e., of variations in the parameters s_1 and s_2 (provided that they both fall in the range $[0.4, 0.6]$). In all cases, we show the final cell pattern (i.e., at $t_f = 60$ days). We constantly employ the initial system configuration shown in Fig. 5, with the parameter values listed in Table 2.

particular, in the latter setting, we have a rate of invasion[3] equal to $\approx$ 125 ± 9.8 μm/month (i.e., $\approx$ 4.16 ± 0.32 μm/day), whereas in the former one such a quantity drops to $\approx$ 65 ± 5.8 μm/month (i.e., $\approx$ 2.1 ± 0.19 μm/day). Finally, when chemotaxis is the solely driving force of cell dynamics, the expansion of lesion is characterized by two distinct phases, see again Fig. 11 (A): (i) during the first two weeks, the tumor quickly enlarges to reach a diameter of 200 ±18 μm (its component cells in fact quickly dissociate being not subjected to adhesive interactions); (ii) for the remaining observation time, the malignant mass follows a linear growth at a rate of $\approx 4.4 \pm 0.39$ μm/day.

The virtual tumor has an invasive fingering morphology when s_1 and s_2 both fall within the range $[0.4, 0.6]$, given their unitary sum. In this spectrum, larger values of s_1 (rsp., lower values of s_2) correspond to thicker and shorter malignant tongues, as shown in Fig. 8 for a pair of representative settings. A dispersed expansion of the lesion instead emerges for $s_1 < 0.4$ (rsp., $s_2 > 0.6$). On the opposite, if $s_1 > 0.6$ (rsp., $s_2 < 0.4$) the malignant mass grows as compact cluster.

Variations in the molecular landscape of the system are in a close correspondence with cell-level dynamics. As displayed in the bottom row of panels in Fig. 7, substantial consumption of oxygen and matrix components in fact occurs in the portion of the tissue invaded by the disease, with inhomogeneities due to the specific rearrangement of the cell configuration. The oxygen profile is typically smoother than the ECM one due to the diffusive behavior of the nutrient. Furthermore, the final density of the matrix is lower in those domain sites occupied by the lesion for a longer time (either by the same cell or by different ones), since we neglect production and diffusion of its components. The ECM pattern indeed gives information not only on the current tumor configuration but also on the past movement of malignant agents. Tumor cells located at the central region of the lesion have a reduced possibility to escape hypoxia also because their migratory capacity is inhibited by the complete degradation of the surrounding matrix (cf. Eq. (6)).

We finally remark that the chemical patterns are not affected by necrotic agents, as they are completely deprived of metabolic activity, and that tumor growth and expansion has not a complete radial symmetry, as different cell and molecular dynamics occur in different regions of the lesion as a consequence of the stochastic aspects included in the model[4]. These considerations will hold in the case of the forthcoming scenarios.

The invasive dynamics of the virtual disease obtained upon variations in the trade-off between adhesiveness and chemotaxis recapitulate a wide spectrum of empirical evidence. More specifically, a fingering morphology is observed to characterize many solid tumors, as displayed in Fig. 9 (A). Malignant masses with unstable ragged fronts are typically more aggressive and hard to be treated than smoother ones: their removal by surgery is in fact difficult, despite their invasive depth is quite limited [143,144]. This last aspect is captured also by our simulations, as it can be assessed by comparing the values of the quantity D in the different scenarios, see Figs. 7 and 11. For the sake of completeness, we remark that the extension of tongues from a progenitor tumor node is reproduced by other individual-based models [73,145]. However, none of these approaches is able to capture the transition from a fingering to a non-fingering tumor morphology upon the variation of a single model parameter.

The morphological and invasive behavior of the tumor mass in the extreme cases, i.e., in the presence of large adhesiveness and poor chemotaxis (or *vice versa*), is instead in a remarkable agreement with the outcomes of a series of *wound healing assays*[5] performed by the group of Prof. Enzo Medico at the Department of Oncological Sciences and Laboratory of Oncogenomics of the Candiolo Institute for Cancer (Torino, Italy). In their experimental protocol, a population of poorly differentiated thyroid carcinoma-derived cells (named ARO) is grown to confluence and then scraped with a pipette tip. Invasive dynamics are observed at 0 and 24 h in the case of two culture conditions, each with a qualitative correspondence to one of our computational scenarios:

1. Control, i.e., absence of any external stimulus. This situation recalls the simulation setting defined by $s_1 = 1$ and $s_2 = 0$. ARO cells are in fact characterized by an intrinsic poor motility and by the tendency to maximize adhesive interactions and to form compact clusters, given the high basal expression and activity of E-cadherin molecules;
2. Stimulation with a nanomolar concentration of hepatocyte growth factor (HGF), which is a ligand able to trigger a sort of mesenchymal transition in ARO cells, as they are induced to loosen contacts, move from their original site, and start wandering in close proximity [160–165]. This second experimental condition

---

[3] The rate of invasion is hereafter calculated as the variation of the Invasive Depth D in a given time lapse.

[4] The radial asymmetry of cell and molecular dynamics is however low enough that there is not a substantial loss of information in reproducing oxygen and ECM profiles only within selected semi-domains.

[5] The wound healing assay is an experimental protocol commonly employed to assess cell motility in bidimensional settings [146–154]. In particular, a cell aggregate is incubated and grown to confluence: an artificial scratch is subsequently created with a sharp object (e.g., a pipette tip) or by other procedures [155,156]. The removal of cells from the wounded area then acts as a stimulus for the remaining mass to fill the open space. The quantification of the recolonized area is used to measure the migratory capacity of the population of interest either in "control/resting conditions" (in serum-deprived medium) or in response to specific chemical stimulations, modifications of the expression of molecules putatively involved in migratory processes, and variations in topological and structural characteristics of the matrix substrates. This last aspect is particularly exploited by biomedical sciences, i.e., in order to produce and test bioengineered scaffolds which provide optimal extracellular environments for regrowth and regeneration of tissues, for example skin, peripheral nerves, bones or cartilage (the literature on this topic is very large, the reader can refer for instance to [157–159] and references therein).

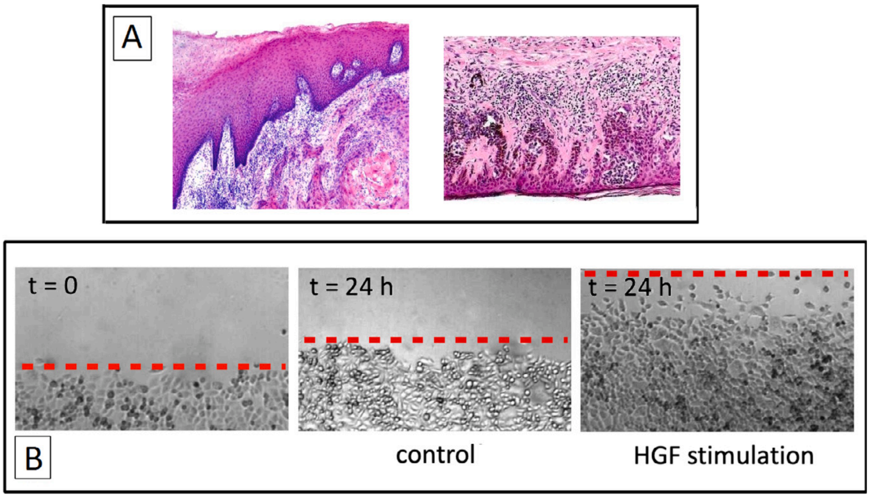

Fig. 9. (A) High-power photomicrographs showing invasive tumors with a fingering morphology. Left panel: squamous cell carcinoma of the tongue. Right panel: lentiginous and junctional moderate melanocytic dysplasia in the epidermis overlying the dermal component. (B) Wound healing assay of a population of ARO cells stimulated with HGF or not (control condition). The experimental images show the initial cell configuration and the final ones (i.e., after 24 h) in the two tested cases. The dashed red lines indicate the actual front of the cell layer. Experimental images are courtesy of the Candiolo Cancer Institute (Torino, Italy).

can be indeed assumed to correspond to the model parameter setting $s_1 = 0$ and $s_2 = 1$.

As shown in Fig. 9 (B), in the absence of HGF, the cell population remains compact over time and a minimal advance of its front is observed: these dynamics agree with those obtained in the corresponding computational scenario (cf. Fig. 7, left column). From the experimental image, we can also notice that cells are overcompressed, due to the formation of stable adhesive junctions which maximize the extension of their contact surfaces. This aspect cannot be reproduced in our model, since our tumor agents are non-deformable elements, each occupying an entire site of the spatial mash, which is fixed over time.

On the opposite, significant invasion of the extracellular space is obtained in the case of chemical stimulation, consistently with the numerical counterpart, cf. Figs. 9 (A) and 7 (right column). In particular, the front of the ARO colony is formed by shed agents, that crawl across the wound and establish the rate of invasion. Cells located far away from the edge of the mass instead display almost negligible displacements. This is due to the well-known mechanism of contact-inhibition of cell locomotion, that is implemented in our model by allowing cell movement only towards free lattice sites. We can finally speculate that, for longer observation times, dissociation would occur also within the central and the rear areas of the experimental cell layer, which therefore would resemble more closely the scattered mass obtained in our model by setting $s_1 = 0$ and $s_2 = 1$.

As a further confirmation of our results, a number of experimental studies demonstrates that down-regulations of cadherin molecules are implicated in a variety of cancers with metastatic potential [166–170]. Furthermore, glioma cell lines are observed to aggressively invade matrix gels in the case of disrupted intercellular adhesiveness; on the opposite, overexpressions of N-cadherins is provided to have a stabilizing effect and to significantly reduce the invasive potential of this type of malignancy [171].

The emergence (and the subsequent extension) of a necrotic core within a malignancy as a consequence of a high and localized oxygen consumption is observed in the case of several tumors grown as spheroids in spinner cultures, such as ovarian [172] or breast [173] carcinomas. Moreover, our model outcomes are consistent with the development of avascular gliomas, both embedded *in vitro* in collagenous gels [174,175] and implanted *in vivo* in mice [6,176], which display a central area of metabolically dead tissue surrounded by a rim of viable (and more motile) cells.

Terminological remark. Hereafter, the simulation setting defined by the model parameters listed in Table 2, the initial system configuration shown in Fig. 3, and by $s_1 = s_2 = 0.5$ will be referred to as the *reference* one.

3.3. Variation in cell proliferation rate

We now evaluate if tumor invasiveness is enhanced by an increment in cell mitotic potential, obtained by setting $\alpha_{DM} = 1$ in Eq. (3). The other model assumptions and parameters are kept unchanged w.r.t. the reference simulation. Malignant agents in a default state have indeed a greater possibility to proliferate: in particular, if normoxic conditions are maintained, all of them certainly undergo duplication within 24 h $(= t_M)$.

For the first two weeks, the tumor is a hyperproliferative mass that expands within the host at an invasive rate close to 7.8 ± 0.75 μm/day, which is higher than the value measured in the reference case, see Figs. 10 and 11 (A). Given unaltered cell migratory ability, invasion is triggered by the growth of the malignant population, as newborn cells occupy space in the surrounding tissue. The larger amount of mitotic events then results in a quick oxygen consumption across the lesion. Both hypoxic and necrotic transitions indeed start nearly two weeks earlier than in the reference simulation, i.e., approximately at 15 (±2) and 30 (±3) days, respectively, as shown in Fig. 10. The metabolically dead core of the disease then rapidly enlarges to occupy, at the end of the observation time, a substantially large portion of the mass (i.e., $I_N \approx 0.26 \pm 0.02$, cf. panel (B) in Fig. 11).

The invasive rate of the tumor reduces to 2.1 ± 0.18 μm/day after the first 15 days, resulting in a final Invasive Depth equal to $\approx 250 \pm 23$ μm, i.e., a value lower than the corresponding quantity obtained in the reference case, see the graphs in Fig. 11. In particular, the front edge of the lesion is composed both of short and thick sprouts and of little islands of malignant cells detached from the main mass, see Fig. 10,

Increments in cell proliferation rate are shown to be necessary but not sufficient to dramatically enhance tumor invasive potential also in experimental models, as in the case of GBP06 and GBP08 colorectal cancer cell lines [142].

The opposite situation, i.e., the inhibition of cell proliferation, could be reproduced in our model by setting $\alpha_{DM} = 0$. However, considering the inclusion of apoptotic processes, this scenario would simply imply a slow but constant loss of volume of the virtual mass until its complete disappearance (not shown).

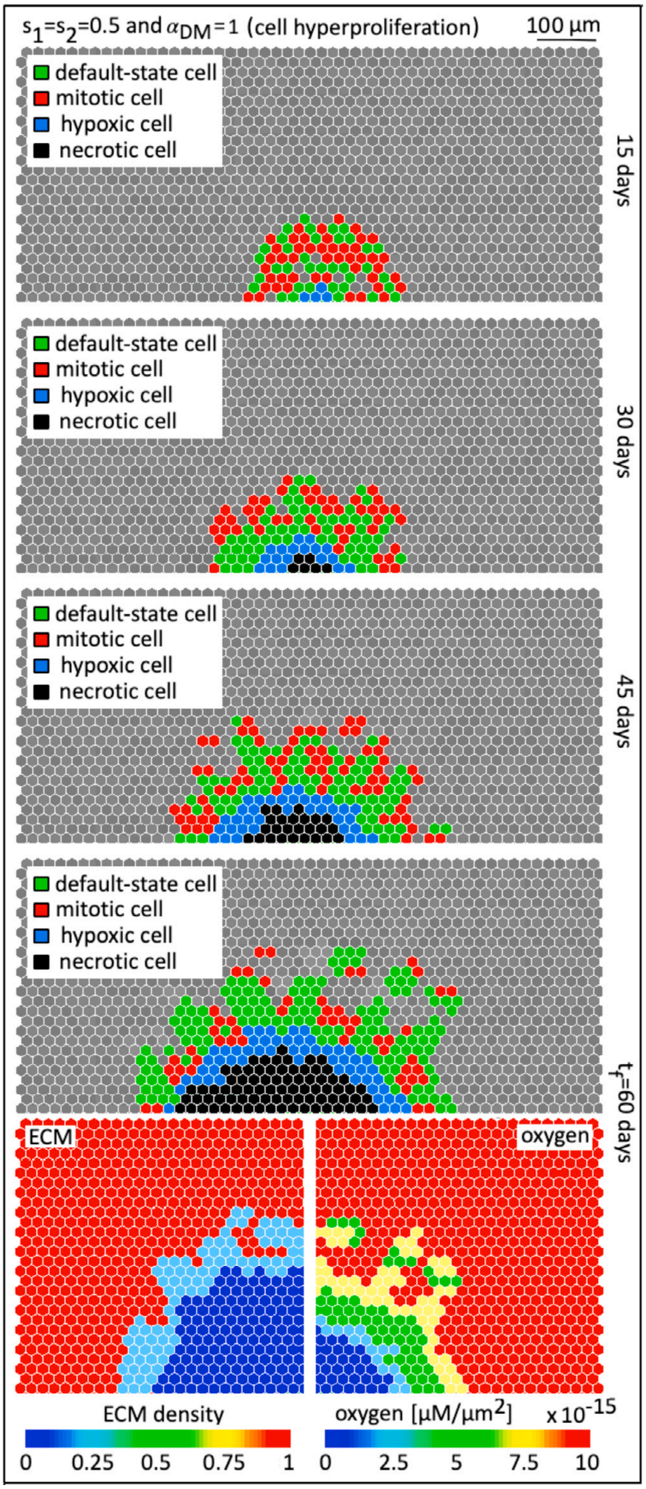

Fig. 10. Tumor growth and progression in the case of enhanced cell proliferation rate, obtained by setting $\alpha_{\rm DM} = 1$ in Eq. (3). The other model assumptions and parameters are kept unchanged w.r.t. the reference simulation. In the bottom panels, we show the final patterns of the ECM density (left semi-domain) and of the oxygen concentration (right semi-domain).

3.4. Disruption of tissue oxygenation

We now assess how tumor progression is shaped by selective environmental pressures. In particular, we analyze the effect of an inadequate environmental oxygenation, obtained by fixing $o^{\rm b} = 0$ in the boundary conditions given in Eq. (11). The remaining model assumptions and parameters are kept unaltered w.r.t. the reference case. The proposed numerical setting indeed models a tissue with a basal level of nutrients (maintained equal to $o^{\rm in}$) but characterized by an inefficient vasculature, that may be due to the presence of blood clots or thrombi.

As shown in Fig. 12, the absence of chemical perfusion accelerates the onset of hypoxic and necrotic processes across the lesion, which start to occur within the first two hours of observation (with a variation in the order of few minutes among the different simulation runs). The available oxygen in fact decays and is quickly absorbed by the tumor, without the possibility of environmental supply. The malignancy then takes approximately 5 h (± 30 min) to become a metabolically dead mass of cells, which may be in principle removed by surgery for the sake of patient's health (cf. Fig. 12, left panels).

These modeling outcomes are in a partial contrast with numerous clinical studies, as hypoxic environmental conditions are widely shown to render malignant cells more aggressive. They are in fact observed to acquire mesenchymal hallmarks, such as the ability to overproduce pro-angiogenic factors and matrix degrading enzymes and to down-express adhesive molecules [177,178], that increase their possibility to escape necrosis, survive, and eventually spread in the surrounding tissue [130,131]. In addition, oxygen deprivation is demonstrated to activate the glycolytic pathway [173], to often induce tumor fragmentation, metastasis and recurrence, and to increase resistance to radiation and chemotherapy [179–181]. Finally, experimental evidence shows that anti-angiogenic therapies may result in the growth of invasive and scattered multifocal lesions [182–185]. In the conclusive section of the work, we will discuss on how these aspects may be accounted in our model.

For the sake of completeness, we then analyze how the virtual mass reacts to a restored oxygenation from the domain border, that is set to occur at $t = 3$ hours, i.e., before its complete necrosis[6]. As shown in the corresponding panels of Fig. 12, a fraction of the lesion, which is in hypoxic conditions but still viable, reacquires a normoxic state. The subsequent dynamics then resemble those observed in the reference case: tongues of malignant cells in fact initiate to form at the edge of the cluster and to infiltrate the host; simultaneously, the necrotic area of the lesion further enlarges, starting from the part that already underwent metabolic death during the inhibition of chemical perfusion. We can indeed affirm that, in our model, a temporary disruption of vascular oxygenation has a small effect on the progression of the disease, at least if chemical supply is restored before the necrosis of the entire tumor mass.

3.5. Variation in the ECM density pattern

We now evaluate the effect on the progression of the disease of a different initial matrix pattern. In particular, as shown in the top panel of Fig. 13, the region of the domain labeled by Ω_1 is characterized by an initial ECM density $e^{\rm in}_{\Omega_1} = 0.5$, that is optimal for cell migration, see Eq. (6). The rest of the tissue, i.e., the region of the domain labeled by Ω_2 $(= \Omega \setminus \Omega_1)$, is instead characterized by the usually high amount of matrix components, i.e., $e^{\rm in}_{\Omega_2} = 1$, that in principle discourages cell movement. The remaining model assumptions and parameters are

---

[6] The critical point is to restore tissue oxygenation before the complete necrosis of the malignant mass, which is observed to occur after approximately 5 h. Given this time lapse, the choice of restoring chemical supply at $t = 3$ hours is arbitrary. Of course, the earlier the oxygenation is restored, the higher the amount of tumor cells still in a metabolically active state is.

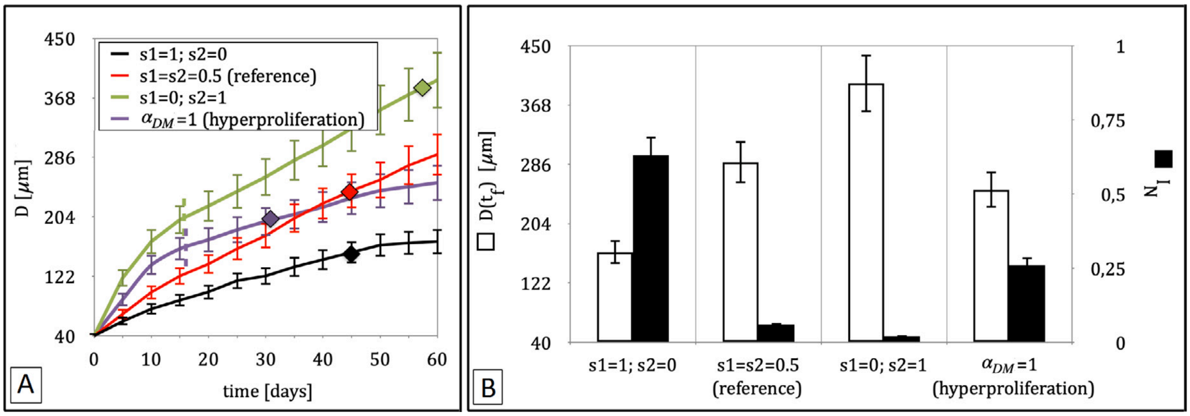

Fig. 11. (A) Time evolution of tumor Invasive Depth, D, evaluated in the different simulation settings described along the text. On each curve, a diamond indicates the mean onset of necrotic processes (i.e., t_n). In the cases of cell hyperproliferation and of absence of adhesion, vertical dashed lines separate an early phase of dramatic expansion of the disease from a later stage of more moderate growth. In the plot, the values of D are the mean calculated over 20 independent numerical realizations, whereas the error bars indicate the standard deviation at some representative time instants. (B) Final Invasive Depth, $D(t_f)$, and Necrotic Index, I_N, evaluated in different scenarios. Each quantity is given as the mean ± the standard deviation calculated over 20 independent simulations.

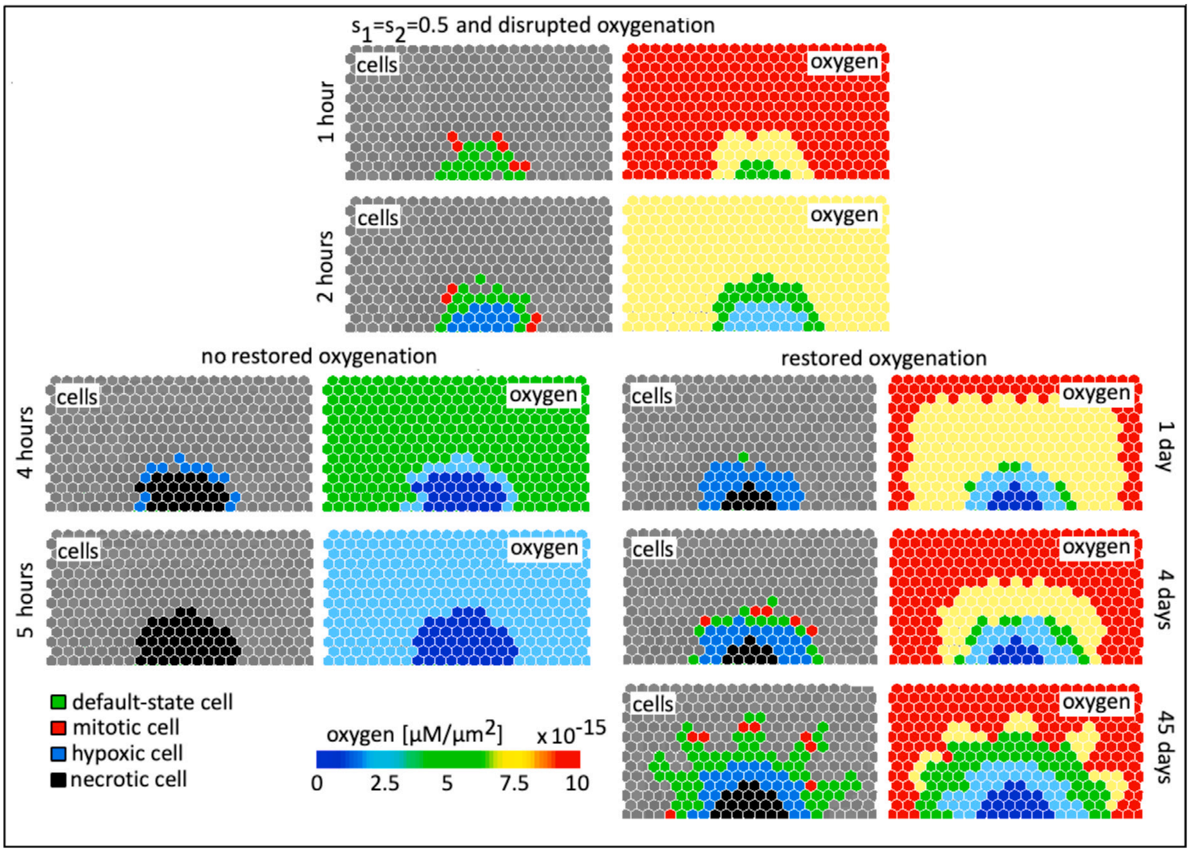

Fig. 12. Tumor growth and progression in the case of disrupted tissue oxygenation, obtained by fixing $o^b = 0$ in the boundary conditions of Eq. (1), that are given in Eq. (11). In the right panels, we represent the dynamics of the malignant mass when a normal vascularization of the tissue is restored at $t = 3$ hours. The other model assumptions and parameters are kept unchanged w.r.t. the reference simulation.

kept unaltered w.r.t. the reference simulation. Tumor growth is then assessed in two scenarios, distinguished by the ability/inability of malignant cells to produce proteolytic enzymes: in particular, the latter case is implemented by setting $\mu_m = 0$ in Eq. (2b), with the obvious implication that the ECM spatial distribution is constant over time.

In the case of MDE inhibition, matrix inhomogeneity strongly shapes tumor growth, as it is possible to observe by the corresponding time-lapse images in Fig. 13. The lesion in fact starts to expand but remains segregated within the region Ω_1, as malignant cells are not able to infiltrate the part of the tissue of high matrix density. Over time, some tumor fingers form and extend from the main core of the disease: however, they are constantly engulfed, since the entire subdomain Ω_1 is progressively filled as a consequence of a sustained cell proliferation. The onset of hypoxic and necrotic processes is substantially delayed w.r.t. the reference case, as the former phenomenon initiates after approximately 45 ± 4 days, whereas the latter one emerges a week later (i.e., at $t_n \approx 52 \pm 5$ days). This is due to the fact that the tumor is characterized by a poor spatial extension and therefore by a limited

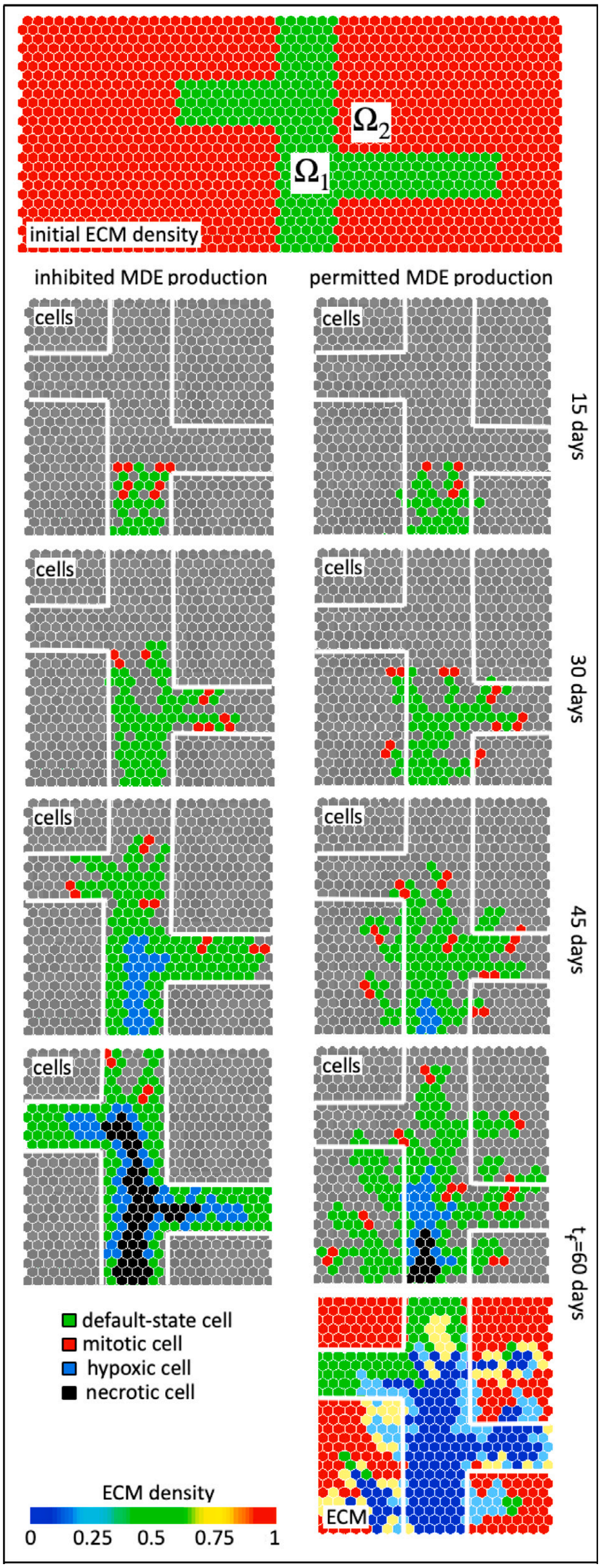

Fig. 13. Tumor growth and progression in the case of a domain differentiated in a region of high matrix density (Ω_2) and in an area with a lower amount of ECM components (Ω_1). In particular, we consider two scenarios defined by the ability/inability of malignant cells to secrete MDEs. The other model assumptions and parameters are kept unchanged w.r.t. the reference simulation. For any reproduced time, we represent the central part of the domain Ω, i.e., where the lesion mainly expands. In the case of the MDE-secreting tumor, we also give the final ECM pattern. In all panels showing a cell configuration, white lines are added to have a rough indication of the extension of the subdomain region Ω_1.

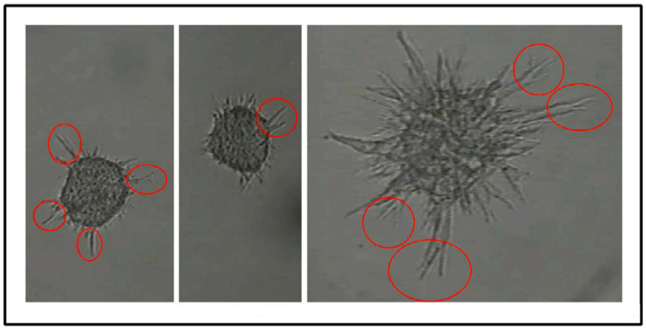

Fig. 14. Spheroids of hepatocellular carcinoma treated with an MMP-inhibitor and cultured in dense matrix gels. As highlighted by the red circles, it is possible to observe thin and long structures protruding from the plasma-membrane of the malignant cells, whose main body remains trapped within the gelatinous medium. Experimental images are courtesy of the Candiolo Cancer Institute (Torino, Italy).

amount of component cells: oxygen consumption is indeed reduced and more efficiently balanced by the diffusion of the chemical from the rest of the tissue, i.e., where it only undergoes a natural decay.

The ability of the tumor to produce matrix degrading enzymes leads to completely different invasive dynamics, see Fig. 13 (right panels). In this case, segregation only characterizes the early progression of the disease. In few days, the malignancy is in fact observed to infiltrate the host also by *de novo* paths generated within the region Ω_2. Along these directions, invasion is however slower, since cells take time to degrade the overdense matrix. Tumor fingers can fully extend and elongate, representing the main invasive structures of the disease. Areas deprived of oxygen emerge across the tumor almost in the same time lapse of the MDE-inhibition case: however, they have a substantially reduced extension, as a consequence of the fact that malignant agents are allowed to more freely move and therefore to have access to a sufficient amount of nutrient. As shown in the bottom-right panel of Fig. 13, at the end of the observation time, the matrix is completely degraded by the proteolytic activity of the disease.

A reduced invasiveness of tumors with disrupted proteolytic activity is also captured by experimental models. For instance, spheroids of malignant cells treated with GM6001 MMP-inhibitor are shown to infiltrate matrix gels with a density that is not hysterically restrictive but to fail to expand within collagen networks characterized by small enough pore size (i.e., by a substantially high density) [139]. In these cases, the component cells in fact protrude towards the surrounding environment with long and thin membrane structures, but their nuclei remain trapped within the mesh of matrix fibers. Examples of this phenomenon are displayed in the experimental images in Fig. 14, that reproduce hepatocellular carcinoma spheroids cultured in three-dimensional dense matrix gels and transfected by an MMP-inhibitor. The creation of secondary infiltration zones by malignant agents with a full proteolytic activity, here seen in the right panels of Fig. 13, are instead described in details in the case both of mouse mammary tumor (MMT) cells [186] and of fibrosarcoma cells [107], placed in 3D collagenous scaffolds and organized in multicellular aggregates.

3.6. Inclusion of cell random crawling

Stochasticity is included in selected state transitions (cf. Eqs. (3), (4), and (5)). It also determines the movement of a cell when the local score $\mathcal{S}$ is simultaneously maximized in a multiplicity of free lattice elements in the neighborhood of its current position. The frequency of this situation is correlated to the trade-off between chemotaxis and adhesiveness: an in-depth analysis of the previous sets of simulations in fact shows that it affects $\approx 25 \pm 3\%$ of cell movement attempts when $s_1 = 0$ and $s_2 = 1$ and $\approx 8 \pm 1\%$ of cell movement attempts when $s_1 > 0$

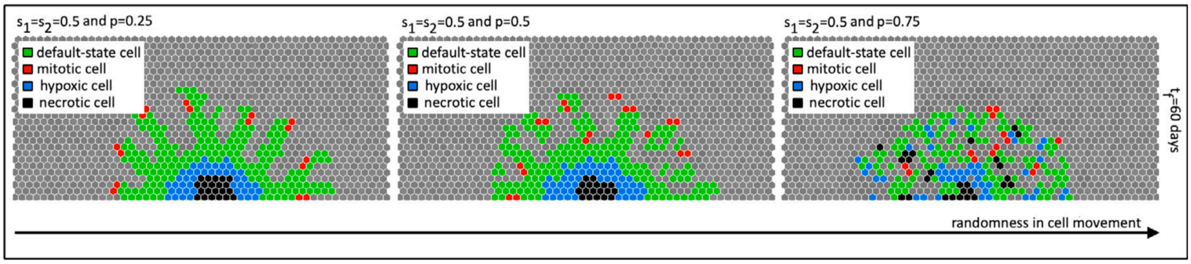

Fig. 15. Tumor growth and progression in the case of the cell migratory law introduced in Eq. (12). The parameter p quantifies the probability of random cell displacements. The other model assumptions and parameters are kept unchanged w.r.t. the reference simulation.

and $s_2 < 1$. The underlying rationale is that when chemotaxis is the unique cell migratory trait, the local score $\mathcal{S}$ is entirely determined by the pattern of oxygen and the distribution of matrix elements (cf. Eq. (6) with $s_1 = 0$) that, especially at the early stages of the evolution of the system, are almost the same across large regions of the domain.

We now increase the relevance of stochastic aspects by varying the rule at the basis of the movement of tumor agents either in the default or in the hypoxic state:

$$\mathbf{x}_t = \begin{cases} \underset{\substack{\{\mathbf{y}\in B_{\mathbf{x}_s}\}\cup\{\mathbf{x}_s\} \\ \mathbf{y}\text{ is free}}}{\arg\max}\ \mathcal{S}(\mathbf{y},t), & \text{with probability } (1-p); \\ \text{a site randomly chosen among the set} & \\ \{\{\mathbf{y}\in B_{\mathbf{x}_s}, \mathbf{y} \text{ is free}\} \cup \{\mathbf{x}_s\}\}, & \text{with probability } p. \end{cases} \tag{12}$$

The parameter p indeed establishes the probability of random cell displacements, i.e., uncorrelated from the value of the local score $\mathcal{S}$ that is, as usual, defined as in Eq. (6). The remaining model assumptions and parameters are kept unaltered w.r.t. the reference case.

From the results in Fig. 15, we can observe that if p is substantially low (i.e., ≤ 0.25), cell dynamics are close to those obtained with the previous movement law (9), i.e., the tumor is characterized by a fingering morphology with necrotic tissue at its center. For intermediate values of $p \in (0.25, 0.75)$, we instead observe the emergence of clumped tumor tongues and the detachment of little clusters of malignant cells from the main mass (cf. central panel in Fig. 15). The frequency of random cell movements in fact increases, thereby preventing the full formation of invasive fingers. A metabolically dead core of agents, surrounded by a hypoxic ring, is still present at the core of the lesion. Finally, when p is large enough (i.e., ≥ 0.75), malignant agents are observed to undergo a sort of Brownian crawling: their behavior is in fact mainly determined by stochasticity and not by the response to internal/environmental stimuli. The tumor indeed becomes a morphologically disorganized and unstable aggregate, with the formation of islands of different dimensions at its external region and of lacunae at its bulk (see Fig. 15, right panel). In this simulation settings, hypoxic and necrotic processes also occur far from the central area of the disease. Tumor cells are in fact not stimulated to escape harsh conditions and move towards tissue regions with higher levels of oxygen. The final invasive depth is reduced, as quantified by a low $D(t_f) = 226 \pm 19$ μm.

4. Discussion and conclusion

We have here reproduced aspects of the avascular growth of a generic solid tumor with a composite multiscale model. Cell dynamics have been described by an individual-based approach, whereas the kinetics of molecular variables (oxygen, soluble ECM components, and tumor-secreted MDEs) by a system of (coupled) reaction diffusion equations, whose source and sink terms have been set to depend on the actual cell configuration, therefore giving rise to a multiscale transmission of information.

More specifically, the malignancy has been assumed to be possibly composed of necrotic and viable individuals, the latter ones in turn differentiated according to their (time-variable) metabolic state. A “Go-or-Grow” hypothesis has been employed to prohibit the movement of cells undergoing proliferation. The other clones of metabolically active cells have been then assumed to move in order to maximize a local score, based on the trade-off between adhesiveness and chemotactic response to oxygen gradients. The local density of the matrix has been also set to affect cell displacements.

Numerical realizations of the proposed model have been then used to assess how the aggressiveness of the disease is influenced by intrinsic and extrinsic factors, the former including manipulations of tumor cell biophysical determinants (adhesiveness, proliferation potential, ability to secrete proteolytic enzymes, frequency of random movements), the latter including variations in the host microenvironment (i.e., oxygenation, initial matrix pattern). Observables relative to the invasive morphology of the tumor and to its internal composition have been evaluated to quantify the results and to facilitate comparison between different scenarios. The standard deviations of these quantities, evaluated over a reasonable number of independent simulations, do not exceed the 15% of the corresponding mean: this is indicative of a substantial robustness of the numerical outcomes, despite the proposed model includes stochastic aspects.

In the next paragraph, the simulation results shown in Section 3 will be reviewed and discussed under the clinical perspective of possible therapeutic interventions.

Biomedical discussion of the proposed computational outcomes. It is nowadays largely recognized that anti-tumoral therapeutic strategies have to treat not only the core of the lesion but also its invasive portion and, in particular, to limit the presence of cells with a high migratory potential [187–190]. Surgical resections of the main malignant mass in fact do not often result in a definitive cure: a fraction of cancer agents may have already invaded surrounding tissues and/or infiltrated the vascular/lymphatic system, incrementing the metastatic potential of the disease and the probability of its recurrence. Cancer cells with a predominant migratory phenotype are also significantly unaffected by conventional cytotoxic treatments, which are instead more efficient against highly proliferating tumor agents [124].

On the basis of these considerations, our simulations have suggested that promising therapeutic interventions should strengthen intercellular adhesiveness and/or reduce cell chemotactic response. In the corresponding numerical settings, the malignant mass has been in fact observed to have compact morphology, poor invasive capacity, and a large portion of necrotic tissue (cf. Figs. 7 and 11).

An increment in cell proliferation potential has been instead shown to have contradictory effects. On one hand, it has enhanced the necrosis of the lesion and limited its invasive distance; on the other hand, the virtual hyperproliferative tumor has displayed a ragged morphology, with the emergence of unstable invasive structures, such as clumped tongues and little islands, whose component cells may have in principle the ability to reach the vasculature and therefore to initiate the metastatic cascade (cf. Figs. 10 and 11). Increments in cell apoptotic rate would certainly imply, in our model, reduced tumor growth and expansion. However, the clinical implementation of this strategy should take into account of possible side-effects, such as a dramatic damage of the normal host tissue.

Our approach has also shown that the progression of a malignant mass is largely affected by selective environmental pressures. In particular, we have predicted that the absence of oxygen supply accelerates and enhances necrotic processes across the tumor, which has been observed to quickly undergo a complete metabolic death (cf. Fig. 12). However, as previously commented, this numerical outcome is not fully consistent with the biomedical paradigm, which rather states that malignant cells in harsh conditions become more aggressive and develop significant resistant to a wide spectrum of clinical interventions, including radiation and chemotherapy. A temporary inhibition of chemical perfusion has been instead observed to have little effect on the simulated tumor dynamics (cf. again Fig. 12).

The numerical results displayed in the previous sections have also shown the potential of clinical interventions that inhibit tumor proteolytic activity: in this case, the malignant mass has been in fact observed to remain segregated within regions of limited matrix density, being unable to invade the areas of the tissue with a high enough presence of ECM components (cf. Fig. 13). Finally, biomedical strategies able to increase the frequency of random cell movements may be in principle relevant from a therapeutic perspective, as demonstrated by the simulations shown in Fig. 15: however, their empirical conceptualization and development are very difficult.

Possible model improvements. The most relevant improvement of our model, according to us, is the inclusion of tumor phenotypic heterogeneity. In the present form of our approach, malignant cells are in fact only differentiated on the basis of their actual metabolic state, but all of them share the same adhesive, migratory, and mitotic determinants, established by common values of s_1, s_2, and α_{DM}, respectively. It is instead widely recognized that, although a malignant lesion is typically formed by cells of the same origin, different subpopulations emerge over time, each with its own biophysical and biochemical characteristics and functions. More specifically, the same disease can be simultaneously composed of cancer cells with full mesenchymal phenotype, i.e., high motility rate and low proliferative potential, and of agents with full epithelial traits, i.e., enhanced mitotic rate and limited migratory capacity [1]. Coexistence and cooperation of these different cell clones are shown to increment the aggressiveness of the entire disease: for instance, highly mitotic cells are able to fuel invasion of more motile agents by exerting oncotic pressure and consuming critical substrates. On the opposite, more invasive cells can open migratory paths for less motile but highly mitotic agents.

Intratumoral heterogeneity may be introduced in our model by assigning each malignant cell i a further state variable, that identifies its current phenotype (i.e., among a given set), say $\tau(i,t) \in \mathcal{T}$. Constitutive laws may then establish a reasonable relation between cell phenotype and behavior, in terms of adhesiveness, chemotactic response, and mitotic rate. For example, given a pair of tumor cells i and j, the former one with mesenchymal traits, i.e., $\tau(i,t)$ =“MES”, and the latter one with an epithelial phenotype, i.e., $\tau(j,t)$ =“EPI”, it may hold that

$$s_1(\tau(i,t)) = s_1(\mathrm{MES}) < s_1(\tau(j,t)) = s_1(\mathrm{EPI}),$$

$$s_2(\tau(i,t)) = s_2(\mathrm{MES}) > s_2(\tau(j,t)) = s_2(\mathrm{EPI}),$$

$$\alpha_{\mathrm{DM}}(\tau(i,t)) = \alpha_{\mathrm{DM}}(\mathrm{MES}) < \alpha_{\mathrm{DM}}(\tau(j,t)) = \alpha_{\mathrm{DM}}(\mathrm{EPI}).$$

The phenotypic state of a cell may be also assumed to vary in time randomly (i.e., mimicking genetic and/or epigenetic mutations) or in response to environmental signals. For instance, the ratio $s_1(\tau(i,t))/s_2(\tau(i,t))$ of a genetic cell i at time t may be set to decrease, thereby favoring chemotaxis w.r.t. adhesiveness, when the agent of interest experiences oxygen deprivation. This way, our virtual hypoxic cells may be facilitated to escape harsh conditions and necrosis, in agreement with the above-cited empirical evidence [191]. Cancer cells use the ability to switch among multiple phenotypes as an evolutionary advantage, i.e., to evade a large spectrum of therapies [192–196]: the proposed model improvement would indeed have a significant clinical relevance.

A different line of model developments may amount in the inclusion of the ECM fibrous component, whose mechanostructural characteristics, e.g., thickness, length, and stiffness, largely affect cell migratory behavior. For instance, several experimental models reveal a cell preference to crawl along aligned matrix fibers, as in the case of fibroblasts cultured in collagen-like gels [108] or of neuronal cells placed on bidimensional fibrin substrates [109]. Cell migratory capacities are also influenced by the deformability of the fiber network, especially in the case of dense matrix meshes which represent a physical obstacle for rigid cells or for cells unable to degrade ECM components, as empirically provided for smooth muscle cells [111], mouse fibroblasts [110], and malignant cells from gliomas [197] and prostate cancers [112]. The local rigidity of the ECM, as well a possible orientation of its component fibers, may be described in our model by the introduction of further matrix-related fields (and corresponding evolution equations). We may also add in Eq. (2a) a term that implements the ability of malignant individuals to depose matrix molecules, as suggested in [198,199].

It would be also relevant to explicitly include in the system normal tissue cells and to model their interactions with the malignant mass. For instance, clusters of tumor cells are shown to displace and compress the surrounding basement membrane and, in the case of carcinomas, the normal epithelium [172]. This way, they create paths of reduced mechanical resistance for infiltration and even extraspace for growth. Recent evidence also demonstrates that tumor cells of epithelial origin are able to induce apoptosis (via acidosis) in the neighboring normal tissue and to alter gene expression in the surrounding stroma, see [200] and references therein. Additional diffusive fields may be added to account for other molecular variables, that may be externally supplied by the host (e.g., vital growth factors or other metabolic nutrients) or expressed/secreted by the malignant mass itself (e.g., waste, products of cell degradation, or angiogenic factors).

The application of the proposed model to a specific type of disease would finally require a proper parametrization, the implementation of a domain configuration able to better describe the tissue of interest, and the use of taylored rules for cell movement, proliferation, and state transitions.

CRediT authorship contribution statement

Marco Scianna: Writing – review & editing, Writing – original draft, Visualization, Validation, Software, Methodology, Investigation, Data curation, Conceptualization.

Declaration of competing interest

I declare to have no conflict of interest relative to the submitted manuscript.

References

[1] D. Hanahan, R.A. Weinberg, Hallmarks of cancer: The next generation, Cell 144 (2011) 646–674.

[2] H. Osada, T. Takahashi, Genetic alterations of multiple tumor suppressors and oncogenes in the carcinogenesis and progression of lung cancer, Oncogene 21 (2002) 7421–7434.

[3] V. Cristini, J.S. Lowengrub, J, Multiscale Modeling of Cancer: An Integrated Experimental and Mathematical Modeling Approach, Cambridge University Press, 2010.

[4] W.F. Mueller-Klieser, R.M. Sutherland, Oxygen consumption and oxygen diffusion properties of multicellular spheroids from two different cell lines, Adv. Exp. Med. Biol. 180 (1984) 311–321.

[5] P. Vaupel, M. Hockel, Blood supply, oxygenation status and metabolic micromilieu of breast cancers: Characterization and therapeutic relevance (review), Int. J. Oncol. 17 (2000) 869–879.

[6] R. Abramovitch, G. Meir, M. Neeman, Neovascularization induced growth of implanted C6 glioma multicellular spheroids: Magnetic resonance microimaging, Cancer Res. 55 (1995) 1956–1962.

[7] J.S. Lowengrub, H.B. Frieboes, F. Jin, Y.L. Chuang, X. Li, P. Macklin, S.M. Wise, V. Cristini, Nonlinear modelling of cancer: Bridging the gap between cells and tumours, Nonlinearity 23 (1) (2010) R1–R9.

[8] P. Mehlen, A. Puisieux, Metastasis: A question of life or death, Nat. Rev. Cancer 6 (2006) 449–458.

[9] G. Murphy, J. Gavrilovic, Proteolysis and cell migration: Creating a path? Curr. Opin. Cell Biol. 11 (1999) 614–621.

[10] W.G. Stetler-Stevenson, S. Aznavoorian, L.A. Liotta, Tumor cell interactions with the extracellular matrix during invasion and metastasis, Ann. Rev. Cell. Biol. 9 (1993) 541–573.

[11] C.C. Maley, A. Aktipis, T.A. Graham, A. Sottoriva, A.M. Boddy, M. Janiszewska, A.S. Silva, M. Gerlinger, Y. Yuan, K.J. Pienta, K.S. Anderson, R. Gatenby, C. Swanton, D. Posada, W. ChungI, J.D. Schiffman, E.S. Hwang, K. Polyak, A.R.A. Anderson, J.S. Brown, M. Greaves, D. Shibata, Classifying the evolutionary and ecological features of neoplasms, Nat. Rev. Cancer 17 (2017) 605–619.

[12] H.M. Byrne, J.R. King, D.L.S. McElwain, L. Preziosi, A two-phase model of solid tumour growth, Appl. Math. Lett. 16 (2003) 567–573.

[13] M.A.J. Chaplain, Avascular growth, angiogenesis and vascular growth in solid tumours: The mathematical modelling of the stages of tumour development, Mathl. Comput. Model. 23 (1996) 47–87.

[14] A. Friedman, F. Reitich, Analysis of a mathematical model for the growth of tumors, J. Math. Biol. 38 (1999) 262–284.

[15] H.P. Greenspan, On the growth and stability of cell cultures and solid tumors, J. Theoret. Biol. 56 (1976) 229–242.

[16] D. Ambrosi, F. Mollica, On the mechanics of a growing tumor, Internat. J. Engrg. Sci. 40 (2002) 1297–1316.

[17] R.P. Araujo, D.L. McElwain, A linear-elastic model of anisotropic tumor growth, Eur. J. Appl. Math. 15 (2004) 365–384.

[18] J.D. Humphrey, Continuum biomechanics of soft biological tissues, Proc. Roy. Soc. Lond. A 459 (2003) 303–311.

[19] A. Menzel, Modelling of anisotropic growth in biological tissues- A new approach and computational aspects, Biomech. Model. Mechanobiol. 3 (2005) 147–171.

[20] T. Roose, P.A. Netti, L.L. Munn, Y. Boucher, R. Jain, Solid stress generated by spheroid growth using a linear poroelastic model, Microvasc. Res. 66 (2003) 204–212.

[21] Y. Kim, M.A. Stolarska, H.G. Othmer, A hybrid model for tumor spheroid growth in vitro: I. Theoretical development and early results, Math. Methods Appl. Sci. 17 (2007) 1773–1798.

[22] B.D. MacArthur, C.P. Please, Residual stress generation and necrosis formation in multi-cell tumour spheroids, J. Math. Biol. 49 (2004) 537–552.

[23] D. Ambrosi, L. Preziosi, Cell adhesion mechanisms and elasto-viscoplastic mechanics of tumours, Mech. Model. Mechanobiol. 8 (2009) 397–413.

[24] P.K. Burgess, P.M. Kulesa, J.D. Murray, E.C. Alvord, The interaction of growth rates and diffusion coefficients in a three dimensional mathematical model of gliomas, J. Neuropathol. Exp. Neurol. 56 (1997) 704–713.

[25] M.A.J. Chaplain, M. Ganesh, I.G. Graham, Spatio-temporal pattern formation on spherical surfaces: Numerical simulation and application to solid tumour growth, J. Math. Biol. 42 (2001) 387–423.

[26] G.C. Cruywagen, D.E. Woodward, P. Tracqui, G.T.P. Bartoo, J.D. Murray, E.C. Alvord, The modeling of diffusive tumors, J. Biol. Syst. 3 (1995) 937–945.

[27] K.R. Swanson, E.C. Alvord, J.D. Murray, A quantitative model for differential motility of gliomas in grey and white matter, Cell Proliferation 33 (2000) 317–329.

[28] H.M. Byrne, M.A. Chaplain, Free boundary value problems associated with the growth and development of multicellular spheroids, Eur. J. Appl. Math. 8 (1997) 639–658.

[29] S. Cui, A. Friedman, A free boundary problem for a singular system of differential equations: An application to a model of tumor growth, Trans. Amer. Math. Soc. 255 (2003) 3537–3590.

[30] G. Pettet, C.P. Please, M. Tindall, D. McElwain, The migration of cells in multicell tumor spheroids, Bull. Math. Biol. 63 (2001) 231–257.

[31] A. Chauviere, T. Hillen, L. Preziosi, Modeling cell movement in anisotropic and heterogeneous tissues, Networks Heterogen. Media 2 (2007) 333–357.

[32] A. Chauviere, L. Preziosi, T. Hillen, Modeling the motion of a cell population in the extracellular matrix, Discrete Contin. Dyn. Syst. B (Suppl) (2007) 250–259.

[33] S. Habib, C. Molina-Paris, T.S. Deisboeck, Complex dynamics of tumors: Modeling an emerging brain tumor system with coupled reaction–diffusion equations, Phys. A Stat. Mech. Appl. 327 (2003) 501–524.

[34] B.P. Marchant, J. Norbury, J.A. Sherratt, Travelling wave solutions to a haptotaxis-dominated model of malignant invasion, Nonlinearity 14 (2001) 1653–1671.

[35] J.A. Sherratt, Traveling wave solutions of a mathematical model for tumor encapsulation, SIAM J. Appl. Math. 60 (1999) 392–407.

[36] H.M. Byrne, M.A.J. Chaplain, Growth of non-necrotic tumors in the presence and absence of inhibitors, Math. Biosci. 130 (1995) 151–181.

[37] V. Cristini, J.S. Lowengrub, Q. Nie, Nonlinear simulation of tumor growth, J. Math. Biol. 46 (2003) 191–224.

[38] H.P. Greenspan, Models for the growth of a solid tumor by diffusion, Stud. Appl. Math. 51 (1972) 317–340.

[39] S.J. Franks, H.M. Byrne, J.R. King, J.C.E. Underwood, C.E. Lewis, Modeling the early growth of ductal carcinoma in situ of the breast, J. Math. Biol. 47 (2003) 424–452.

[40] S.J. Franks, J.R. King, Interactions between a uniformly proliferating tumor and its surrounding uniform material properties, Math. Med. Biol. 20 (2003) 47–89.

[41] J. Wu, S. Cui, Asymptotic behavior of solutions of a free boundary problem modeling the growth of tumors with stokes equations, Discrete Contin. Dyn. Syst. 24 (2009) 625–651.

[42] X. Zheng, S. Wise, V. Cristini, Nonlinear simulation of tumor necrosis, neovascularization and tissue invasion via an adaptive finite-element/level-set method, Bull. Math. Biol. 67 (2005) 211–259.

[43] A.R. Anderson, A. Weaver, P. Commmings, V. Quaranta, Tumor morphology and phenotypic evolution driven by selective pressure from the microenvironment, Cell 127 (2006) 905–915.

[44] H.M. Byrne, P. Matthews, Asymmetric growth of models of avascular solid tumors: Exploiting symmetries, IMA J. Math. Appl. Med. Biol. 19 (2002) 1–29.

[45] C.S. Hogea, B.T. Murray, J.A. Sethian, Simulating complex tumor dynamics from avascular to vascular growth using a general level-set method, J. Math. Biol. 53 (2006) 86–134.

[46] C.P. Please, G.J. Pettet, D.L.S. McElwain, A new approach to modeling the formation of necrotic regions in tumors, Appl. Math. Lett. 11 (1998) 89–94.

[47] H.M. Byrne, M.A.J. Chaplain, Mathematical models for tumour angiogenesis: Numerical simulations and nonlinear wave solutions, Bull. Math. Biol. 57 (1995) 461–486.

[48] H.A. Levine, S. Pamuk, B.D. Sleeman, M. Nilsen-Hamilton, Mathematical modeling of capillary formation and development in tumor angiogenesis: Penetration into the stroma, Bull. Math. Biol. 63 (2001) 801–863.

[49] H.A. Levine, B.D. Sleeman, M. Nilsen-Hamilton, Mathematical modeling of the onset of capillary formation initiating angiogenesis, J. Math. Biol. 42 (2001) 195–238.

[50] H.A. Levine, A.L. Tucker, M.A. Nilsen-Hamilton, A mathematical model for the role of cell signal transduction in the initiation and inhibition of angiogenesis, Growth Factors 20 (2002) 155–175.

[51] M.E. Orme, M.A. Chaplain, Two-dimensional models of tumour angiogenesis and anti-angiogenesis strategies, Math. Med. Biol. 14 (1997) 189–205.

[52] R.P. Araujo, D.L. McElwain, A mixture theory for the genesis of residual stresses in growing tissues: A general formulation, SIAM J. Appl. Math. 65 (2005) 1261–1284.

[53] R.P. Araujo, D.L. McElwain, A mixture theory for the genesis of residual stresses in growing tissues: II. Solutions to the biphasic equations for a multicell spheroid, SIAM J. Appl. Math. 66 (2005) 447–467.

[54] H.M. Byrne, L. Preziosi, Modelling solid tumour growth using the theory of mixtures, Math. Med. Biol. 20 (2003) 341–366.

[55] M.A.J. Chaplain, L. Graziano, L. Preziosi, Mathematical modelling of the loss of tissue compression responsiveness and its role in solid tumor development, Math. Med. Biol. 23 (2006) 197–229.

[56] S.R. Lubkin, T.L. Jackson, Multiphase mechanics of capsule formation in tumors, J. Biomed. Eng.– Trans. ASME 124 (2002) 237–243.

[57] A. Bertuzzi, A. Fasano, A. Gandolfi, C. Sinisgalli, Atp production and necrosis formation in a tumour spheroid model, Math. Model. Natural Phenom. 2 (2007) 30–46.

[58] C.P. Please, G.J. Pettet, D.L.S. McElwain, Avascular tumour dynamics and necrosis, Math. Models Appl. Sci. 9 (1999) 569–579.

[59] J.P. Ward, J.R. King, Mathematical modelling of avascular-tumour growth, Math. Med. Biol.: J. IMA 14 (1997) 39–69.

[60] J.P. Ward, J.R. King, Mathematical modelling of avascular-tumour growth: II. Modelling growth saturation, Math. Med. Biol. 16 (1999) 171–211.

[61] B. Perthame, Transport Equations in Biology, Birkh́auser Verlag, Basel, 2007.

[62] R.A. Gatenby, B.R. Frieden, Application of information theory and extreme physical information to carcinogenesis, Cancer Res. 62 (2002) 2684–3675.

[63] R.A. Gatenby, T.L. Vincent, An evolutionary model of carcinogenesis, Cancer Res. 63 (2003) 6212–6220.

[64] M.S. Alber, M.A. Kiskowski, J.A. Glazier, Y. Jiang, in: R. Rosenthal, D.S. Gilliam (Eds.), On Cellular Automaton Approaches to Modeling Biological Cells, in: IMA Series On Mathematical Systems Theory in Biology, Communication and Finance, vol. 142, Springer, New York, 2002, pp. 1–40.

[65] A.R. Anderson, M.J. Chaplain, K.A. Rejniak (Eds.), Single-Cell-Based Models in Biology and Medicine, in: Mathematics and Biosciences in Interactions, Birḱauser, Basel, 2007.

[66] A.R. Anderson, V. Quaranta, Integrative mathematical oncology, Nat. Rev. Cancer 8 (2008) 227–234.

[67] D. Drasdo, in: W. Alt, et al. (Eds.), On Selected Individual-Based Approaches to the Dynamics of Multicellular Systems Multiscale Modeling, Birkhauser, Basel, 2003.

[68] J. Galle, G. Aust, G. Schaller, T. Beyer, D. Drasdo, Individual cell-based models of the spatial temporal organization of multicellular systems-achievements and limitations, Cytometry 69 (A) (2006) 704–710.

[69] J. Moreira, A. Deutsch, Cellular automaton models of tumor development: A critical review, Adv. Complex Syst. 5 (2002) 247–267.

[70] D. Drasdo, S. H´ohme, Individual-based approaches to birth and death in avascular tumors, Math. Comput. Modelling 37 (2003) 1163–1175.

[71] D. Drasdo, R. Kree, J.S. McCaskill, Monte Carlo approach to tissue cell populations, Phys. Rev. E 52 (1995) 6635–6657.

[72] A. Shirinifard, J.S. Gens, B.L. Zaitlen, N.J. Poplawski, M. Swat, J.A. Glazier, 3D multi-cell simulation of tumor growth and angiogenesis, PLoS One 4 (2009) e7190.

[73] S. Turner, J.A. Sherratt, Intercellular adhesion and cancer invasion: A discrete simulation using the extended Potts model, J. Theoret. Biol. 216 (1) (2002) 85–100.

[74] A.R. Anderson, M.A. Chaplain, Continuous and discrete mathematical models of tumor-induced angiogenesis, Bull. Math. Biol. 60 (1998) 857–899.

[75] M.J. Plank, B.D. Sleeman, A reinforced random walk model of tumour angiogenesis and anti-angiogenic strategies, Math. Med. Biol. 20 (2003) 135–181.

[76] M.J. Plank, B.D. Sleeman, Lattice and non-lattice models of tumour angiogenesis, Bull. Math. Biol. 66 (2004) 1785–1819.

[77] C.L. Stokes, D.A. Lauffenburger, Analysis of the roles of microvessel endothelial cell random motility and chemotaxis in angiogenesis, J. Theoret. Biol. 152 (1991) 377–403.

[78] S. Sun, M.F. Wheeler, M. Obeyesekere, C.W. Patrick, Multiscale angiogenesis modeling using mixed finite element methods, Multiscale Model. Simul. 4 (2005) 1137–1167.

[79] S. Sun, M.F. Wheeler, M. Obeyesekere, C.W. Patrick, A deterministic model of growth factor-induced angiogenesis, Bull. Math. Biol. 67 (2005) 313–337.

[80] M.A. Stolarska, Y. Kim, H.G. Othmer, Multiscale models of cell and tissue dynamics, Phil. Trans. R. Soc. A 367 (2009) 3525–3553.

[81] E.L. Bearer, J.S. Lowengrub, Y.L. Chuang, H.B. Frieboes, F. Jin, S.M. Wise, M. Ferrari, D.B. Agus, V. Cristini, Multiparameter computational modeling of tumor invasion, Cancer Res. 69 (2009) 4493–44501.

[82] D. Drasdo, S. H´ohme, A single-scale-based model of tumor growth in vitro: Monolayers and spheroids, Phys. Biol. 2 (2005) 133–147.

[83] J. Clairambault, Modelling physiological and pharmacological control on cell proliferation to optimise cancer treatments, Math. Model. Nat. Phenom. 4 (2009) 12–67.

[84] A. Friedman, Free boundary problems associated with multiscale tumor models, Math. Model. Nat. Phenom. 4 (2009) 134–155.

[85] M. Doumic, Analysis of a population model structured by the cells molecular content, Math. Model. Nat. Phenom. 2 (2007) 121–152.

[86] I. Ramis-Conde, D. Drasdo, A.R.A. Anderson, M.A.J. Chaplain, Modeling the influence of E-Cadherin-beta-catenin pathway in cancer cell invasion: A multiscale approach, Biophys. J. 95 (2008) 155–165.

[87] A.R. Anderson, K. Rejniak, P. Gerlee, V. Quaranta, Microenvironment driven invasion: A multiscale multimodel investigation, J. Math. Biol. 58 (2009) 579–624.

[88] K. Rejniak, A single-cell approach in modeling the dynamics of tumor microregions, Math. Biosci. Eng. 2 (2005) 643–655.

[89] K. Rejniak, An immersed boundary framework for modeling the growth of individual cells: An application to the early tumour development, J. Theoret. Biol. 247 (2007) 186–204.

[90] K. Rejniak, A.R.A. Anderson, A computational study of the development of epithelial acini: I. Sufficient conditions for the formation of a hollow structure, Bull. Math. Biol. 70 (2008) 677–712.

[91] K. Rejniak, A.R.A. Anderson, A computational study of the development of epithelial acini: II. Necessary conditions for structure and lumen stability, Bull. Math. Biol. 70 (2008) 1450–1479.

[92] K. Rejniak, R. Dillon, A single cell-based model of the ductal tumor microarchitecture, Comput. Math. Methods Med. 8 (2007) 51–69.

[93] Y. Jiang, J. Pjesivac-Grbovic, C. Cantrell, J. Freyer, A multiscale model for avascular tumor growth, Biophys. J. 89 (2005) 3884–3894.

[94] E.L. Stott, N. Britton, J.A. Glazier, M. Zajac, Simulation of benign avascular tumour growth using the Potts model, Math. Comput. Modelling 30 (1999) 183–198.

[95] J.A. Adam, General aspects of modeling tumor growth and immune response, in: A Survey of Models for Tumor-Immune System Dynamics, Springer, 2007, pp. 15–87.

[96] A.R. Anderson, M.A. Chaplain, E.L. Newman, R.J. Steele, A.M. Thompson, Mathematical modelling of tumour invasion and metastasis, Comput. Math. Methods Med. 2 (2000) 129–154.

[97] R.P. Araujo, D.L. McElwain, A history of the study of solid tumour growth: The contribution of mathematical modelling, Bull. Math. Biol. 66 (2004) 1039–1091.

[98] P.K. N. Bellomo, Maini, On the foundations of cancer modelling: Selected topics, speculations, and perspectives, Math. Models Methods Appl. Sci. 18 (2008) 593–646.

[99] N. Bellomo, L. Preziosi, Modelling and mathematical problems related to tumor evolution and its interaction with the immune system, Math. Comput. Modelling 32 (2000) 413–452.

[100] H.M. Byrne, T. Alarcon, M.R. Owen, S.D. Webb, P.K. Maini, Modelling aspects of cancer dynamics: A review, Phil. Trans. R. Soc. A 364 (2006) 1563–1578.

[101] M.A.J. Chaplain, A.R.A. Anderson, Mathematical modelling of tissue invasion, in: L. Preziosi (Ed.), Cancer Modelling and Simulation, Chapman Hall/CRC Press, 2003, pp. 269–297.

[102] R. Eftimie, J.L. Bramson, D.J. Earn, Interactions between the immune system and cancer: A brief review of non-spatial mathematical models, Bull. Math. Biol. 73 (2011) 2–32.

[103] A. Friedman, A hierarchy of cancer models and their mathematical challenges, Discrete Contin. Dynam. Syst.–B 4 (1) (2004) 147–159.

[104] A. Friedman, Mathematical analysis and challenges arising from models of tumor growth, Math. Models Methods Appl. Sci. 17 (2007) 1751–1772.

[105] D. Trucu, P. Domschke, A. Gerisch, M.A. Chaplain, Multiscale computational modelling and analysis of cancer invasion, in: L. Preziosi, M.A. Chaplain, A. Pugliese, A. (Eds.), Mathematical Models and Methods for Living Systems, in: Lecture Notes in Mathematics, vol. 2167, Springer, Cham. Edinburgh, 2016, pp. 275–321.

[106] K.B. Hotary, E.D. Allen, P.C. Brooks, N.S. Datta, M.W. Long, S.J. Weiss, Membrane type I matrix metalloproteinase usurps tumor growth control imposed by the three–dimensional extracellular matrix, Cell 114 (2003) 33–45.

[107] K. Wolf, Y.I. Wu, Y. Liu, J. Geiger, E. Tam, Multi-step pericellular proteolysis controls the transition from individual to collective cancer cell invasion, Nat. Cell. Biol. 9 (2007) 893–904.

[108] R.B. Dickinson, S. Guido, R.T. Tranquillo, Biased cell–migration of fibroblasts exhibiting contact guidance in oriented collagen gels, Ann. Biomed. Eng. 22 (1994) 342–356.

[109] N. Dubey, P.C. Letourneau, R.T. Tranquillo, Neuronal contact guidance in magnetically aligned fibrin gels: Effect of variation in gel mechano–structural properties, Biomaterials 22 (2001) 1065–1075.

[110] B.A. Harley, H. Kim, M.H. Zaman, I.V. Yannas, D.A. Lauffenburger, L.J. Gibson, Microarchitecture of three-dimensional scaffolds influences cell migration behavior via junction interactions, Biophys. J. 95 (8) (2008) 4013–4024.

[111] S.R. Peyton, A.J. Putnam, Extracellular matrix rigidity governs smooth muscle cell motility in a biphasic fashion, J. Cell Physiol. 204 (2005) 198–209.

[112] M.H. Zaman, L.M. Trapani, A.L. Sieminski, D. Mackellar, H. Gong, R.D. Kamm, A. Wells, D.A. Lauffenburger, P. Matsudaira, Migration of tumor cells in 3D matrices is governed by matrix stiffness along with cell–matrix adhesion and proteolysis, Proc. Natl. Acad. Sci. USA 103 (29) (2006) 10889–10894.

[113] B.W. Pogue, J.A. O'Hara, C.M. Wilmot, K.D. Paulsen, H.M. Swartz, Estimation of oxygen distribution in RIF-1 tumors by diffusion model-based interpretation of pimonidazole hypoxia and Eppendorf measurements, Radiat. Res. 155 (2001) 15–25.

[114] I.F. Tannock, Oxygen diffusion and the distribution of cellular radiosensitivity in tumours, Brit. J. Radiol. 45 (1972) 515–524.

[115] A.I. McClatchey, A.S. Yap, Contact inhibition (of proliferation) redux, Curr. Opin. Cell Biol. 24 (2012) 685–694.

[116] P. Friedl, K. Wolf, Tumour–cell invasion and migration: Diversity and escape mechanisms, Nat. Rev. Cancer 3 (2003) 362–374.

[117] S.L. Goodman, G. Risse, K. Vondermark, The E8 subfragment of laminin promotes locomotion of myoblasts over extracellular matrix, J. Cell. Biol. 109 (1989) 799–809.

[118] M. Arnold, V.C. Hirschfeld-Warneken, T. Lohmuller, P. Heil, J. Blummel, E.A. Cavalcanti-Adam, M. Lopez-Garcia, P. Walther, H. Kessler, B. Geiger, J.P. Spatz, Induction of cell polarization and migration by a gradient of nanoscale variations in adhesive ligand spacing, Nano Lett. 8 (2008) 2063–2069.

[119] E.A. Cavalcanti-Adam, T. Volberg, A. Micoulet, H. Kessler, B. Geiger, J.P. Spatz, Cell spreading and focal adhesion dynamics are regulated by spacing of integrin ligands, Biophys. J. 92 (2007) 2964–2974.

[120] P. Friedl, K. Maaser, C.E. Klein, B. Niggemann, G. Krohne, K.S. Zanker, Migration of highly aggressive MV3 melanoma cells in 3-dimensional collagen lattices results in local matrix reorganization and shedding of alpha2 and beta1 integrins and CD44, Cancer Res. 57 (1997) 2061–2070.

[121] E. Lamers, R. Van Horssen, J. Te Riet, F.C. Van Delft, R. Luttge, X.F. Walboomers, J.A. Jansen, The influence of nanoscale topographical cues on initial osteoblast morphology and migration, Eur. Cell. Mater. 9 (2010) 329–343.

[122] A. Engler, L. Bacakova, C. Newman, A. Hategan, M. Griffin, D. Discher, Substrate compliance versus ligand density in cell on gel responses, Biophys. J. 86 (2004) 617–628.

[123] C. Gaudet, W. Marganski, S. Kim, C.T. Brown, V. Gunderia, M. Dembo, J. Wong, Influence of type I collagen surface density on fibroblast spreading, motility, and contractility, Biophys. J. 85 (2003) 3329–3335.

[124] A. Giese, L. Kluwe, B. Laube, H. Meissner, M.E. Berens, M. Westphal, Migration of human glioma cells on myelin, Neurosurgery 38 (1996) 755–764.

[125] A. Giese, M.A. Loo, N. Tran, D. Haskett, S.W. Coons, M.E. Berens, Dichotomy of astrocytoma migration and proliferation, Int. J. Cancer 67 (1996) 275–282.

[126] J.A. Gallaher, J.S. Brown, A.R.A. Anderson, The impact of proliferation–migration tradeoffs on phenotypic evolution in cancer, Sci. Rep. 9 (2019) 1–10.

[127] H. Hatzikirou, D. Basanta, M. Simon, K. Schaller, A. Deutsch, “Go or grow”: The key to the emergence of invasion in tumour progression? Math. Med. Biol.: J. IMA 29 (2012) 49–65.

[128] A. Martínez-González, G.F. Calvo, L.A. Pérez Romasanta, V.M. Pérez-García, Hypoxic cell waves around necrotic cores in glioblastoma: A biomathematical model and its therapeutic implications, Bull. Math. Biol. 74 (2012) 2875–2896.

[129] K.R. Swanson, R.C. Rockne, J. Claridge, M.A. Chaplain, E.C. Alvord, A.R.A. Anderson, Quantifying the role of angiogenesis in malignant progression of gliomas: In silico modeling integrates imaging and histology, Cancer Res. 71 (2011) 7366–7375.

[130] H.N. Barrak, A.K. Maitham, Y.A. Luqmani, Hypoxic environment may enhance migration/penetration of endocrine resistant MCF7-derived breast cancer cells through monolayers of other non-invasive cancer cells in vitro, Sci. Rep. 10 (1) (2020) 1–14.

[131] S.-H. Kao, K.-J. Wu, W.-H. Lee, Hypoxia, epithelial-mesenchymal transition, and TET-mediated epigenetic changes, J. Clin. Med. 5 (2) (2016) 24–38.

[132] B. Alberts, A.D. Johnson, J. Lewis, M. Raff, K. Roberts, P. Walter, Molecular Biology of the Cell, Garland Science, New York, 2002.

[133] M. Beil, A. Micoulet, G. Wichert, S. Paschke, P. Walther, et al., Sphingosylphosphorylcholine regulates keratin network architecture and viscoelastic properties of human cancer cells, Nat. Cell Biol. 5 (2003) 803–811.

[134] C.G. Rolli, T. Seufferlein, R. Kemkemer, J.P. Spatz, Impact of tumor cell cytoskeleton organization on invasiveness and migration: A microchannel–based approach, PLoS One 5 (2010) e8726.

[135] G. Chiari, M. Delitala, D. Morselli, M. Scianna, A hybrid modeling environment to describe aggregates of cells heterogeneous for genotype and behavior with possible phenotypic transitions, Int. J. Non–Linear Mech. 144 (2022) 104063.

[136] P. Cumsille, A. Coronel, C. Conca, C. Quiñinao, C. Escudero, Proposal of a hybrid approach for tumor progression and tumor-induced angiogenesis, Theor. Biol. Med. Model. 12 (13) (2015) 1–22.

[137] J.P. Freyer, R.M. Sutherland, Determination of diffusion constants for metabolites in multicell tumor spheroids, Adv. Exp. Med. Biol. 159 (1983) 463–475.

[138] J.P. Freyer, R.M. Sutherland, Regulation of growth saturation and development of necrosis in EMT6/Ro multicellular spheroids by the glucose and oxygen supply, Cancer Res. 46 (1986) 3504–3512.

[139] K. Wolf, M. te Lindert, M. Krause, S. Alexander, J. te Riet, A.L. Willis, R.M. Hoffman, C.G. Figdor, S.J. Weiss, P. Friedl, Physical limits of cell migration: Control by ECM space and nuclear deformation and tuning by proteolysis and traction force, J. Cell Biol. 201 (2013) 1069–1084.

[140] J. Steinbach, H. Wolburg, A. Klumpp, A., et al., Hypoxia-induced cell death in human malignant glioma cells: Energy deprivation promotes decoupling of mitochondrial cytochrome c release from caspase processing and necrotic cell death, Cell Death Differ. 10 (2003) 823–832.

[141] J.M. Brown, W.R. Wilson, Exploiting tumour hypoxia in cancer treatment, Nat. Rev. Cancer 4 (2004) 437–447.

[142] M.E. Oraiopoulou, E. Tzamali, G. Tzedakis, A. Vakis, J. Papamatheakis, V. Sakkalis, In vitro/in silico study on the role of doubling time heterogeneity among primary glioblastoma cell lines, Biomed. Res. Int. (2017) 8569328.

[143] S.S. Cross, Fractals in pathology, J. Pathol. 182 (1997) 1–8.

[144] G. Landini, Y. Hirayama, T.J. Li, M. Kitano, Increased fractal complexity of the epithelial connective tissue interface in the tongue of 4NQ0–Treated rats, Pathol. Res. Pract. 196 (2000) 251–258.

[145] J. Smolle, Fractal tumor stromal border in a nonequilibrium growth model, Anal. Quant. Cytol. Histol. 20 (1998) 7–13.

[146] W. Bement, P. Forscher, M.A. Mooseker, A novel cytoskeletal structure involved in purse string wound closure and cell polarity maintenance, J. Cell Biol. 121 (1993) 565–578.

[147] E.R. Block, A.R. Matela, N. Sundar Raj, E.R. Iszkula, J.K. Klarlund, Wounding induces motility in sheets of corneal epithelial cells through loss of spatial constraints, roles of heparin-binding epidermal growth factor-like signaling, J. Biol. Chem. 279 (2004) 24307–24312.

[148] J. Brock, K. Midwinter, J. Lewis, P. Martin, Healing of incisional wounds in the embryonic chick wing bud: Characterization of the actin purse–string and demonstration of a requirement for Rho activation, J. Cell Biol. 135 (1996) 1097–1107.

[149] R. Farooqui, G. Fenteany, Multiple rows of cells behind an epithelial wound edge extend cryptic lamellipodia to collectively drive cell sheet movement, J. Cell Sci. 118 (2005) 51–63.

[150] P. Martin, J. Lewis, Actin cables and epidermal movement in embryonic wound healing, Nature 360 (1992) 179–183.

[151] P. Martin, Wound healing–aiming for perfect skin regeneration, Science 276 (1997) 75–81.

[152] M. Poujade, E. Grasland-Mongrain, A. Hertzog, J. Jouanneau, P. Chavrier, B. Ladoux, A. Buguin, P. Silberzan, Collective migration of an epithelial monolayer in response to a model wound, Proc. Natl. Acad. Sci. USA 104 (2007) 15988–15993.

[153] K. Suzuki, J. Saito, R. Yanai, N. Yamada, T. Chikama, K. Seki, T. Nishida, Cell–matrix and cell–cell interactions during corneal epithelial wound healing, Prog. Retin. Eye Res. 22 (2003) 113–133.

[154] K.P. Xu, Y. Ding, J. Ling, Z. Dong, F.S. Yu, Wound-induced HB-EGF ectodomain shedding and EGFR activation in corneal epithelial cells, Invest. Ophthalmol. Vis. Sci. 45 (2004) 813–820.

[155] E. Fong, S. Tzlilb, D.A. Tirrell, Boundary crossing in epithelial wound healing, Proc. Natl. Acad. Sci. USA 107 (2010) 19302–19307.

[156] D.L. D. L. Nikolić, A.N. Boettiger, D. Bar-Sagi, J.D. Carbeck, S.Y. Shvartsman, Role of boundary conditions in an experimental model of epithelial wound healing, Am. J. Physiol. Cell Physiol. 291 (2006) C68–C75.

[157] R.M. Capito, M. Spector, Scaffold-based articular cartilage repair, IEEE Eng. Med. Biol. Mag. 22 (2003) 42–50.

[158] C. Spadaccio, A. Rainer, S. De Porcellinis, M. Centola, F. De Marco, M. Chello, M. Trombetta, J.A. Genovese, A G-CSF functionalized PLLA scaffold for wound repair: An in vitro preliminary study, in: Conf. Proc. IEEE Eng. Med. Biol. Soc., 2010, pp. 843–846.

[159] I.V. Yannas, E. Lee, D.P. Orgill, E.M. Skrabut, G.F. Murphy, Synthesis and characterization of a model extracellular matrix that induces partial regeneration of adult mammalian skin, Proc. Natl. Acad. Sci. USA 86 (1989) 933–937.

[160] K. Matsumoto, T. Nakamura, NK4 gene therapy targeting HGF–Met and angiogenesis, Front. Biosci. 13 (2008) 1943–1951.

[161] T. Nakamura, H. Teramoto, A. Ichihara, Purification and characterization of a growth factor from rat platelets for mature parenchymal hepatocytes in primary cultures, Proc. Natl. Acad. Sci. USA 83 (1986) 6489–6493.

[162] H. Sakata, S.J. Stahl, W.G. Taylor, J.M. Rosenberg, K. Sakaguchi, P.T. Wingfield, J.S. Rubin, Heparin binding and oligomerization of hepatocyte growth factor/scatter factor isoforms, J. Biol. Chem. 272 (1997) 9457–9463.

[163] M. Stoker, E. Gherardi, M. Perryman, J. Gray, Scatter factor is a fibroblast-derived modulator of epithelial cell mobility, Nature 21 (6119) (1987) 239–242.

[164] L. Tamagnone, P.M. Comoglio, Control of invasive growth by Hepatocyte Growth Factor (HGF) and related scatter factors, Cytokine Growth Factor Rev. 8 (2) (1997) 129–142.

[165] L. Trusolino, P.M. Comoglio, Scatter-factor and semaphorin receptors: Cell signalling for invasive growth, Nat. Rev. Cancer 2 (4) (2002) 289–300.

[166] U. Cavallaro, G. Christofori, Cell adhesion in tumor invasion and metastasis: Loss of the glue is not enough, Biochim. Biophys. Acta 1552 (2001) 39–45.

[167] U. Cavallaro, G. Christofori, Cell adhesion and signalling by cadherins and Ig–CAMs in cancer, Nat. Rev. Cancer 4 (2004) 118–132.

[168] G. Christofori, Changing neighbours, changing behaviour: Cell adhesion molecule–mediated signalling during tumour progression, EMBO J. 22 (2003) 2318–2323.

[169] K. Sundfeldt, Cell–cell adhesion in the normal ovary and ovarian tumors of epithelial origin; An exception to the rule, Mol. Cell. Endocrinol. 202 (2003) 89–96.

[170] K. Vleminckx, L. Vakaet, M. Mareel, W. Fiers, F. Vanroy, Genetic manipulation of E-cadherin expression by epithelial tumor cells reveals an invasion suppressor role, Cell 66 (1991) 107–119.

[171] B. Hegedus, F. Marga, K. Jakab, K.L. Sharpe-Timms, G. Forgacs, The interplay of cell–cell and cell–matrix interactions in the invasive properties of brain tumors, Biophys. J. 91 (2006) (2006) 2708–2716.

[172] K. Shield, M.L. Ackland, N. Ahnmed, G.E. Rice, Multicellular spheroids in ovarian cancer metastases: Biology and pathology, Gynec. Oncol. 113 (2008) 143–148.

[173] R.A. Gatenby, K. Smallbone, P.K. Maini, F. Rose, J. Averill, R. Nagle, L. Worrall, R. Gillies, Cellular adaptations to hypoxia and acidosis during somatic evolution of breast cancer, Br. J. Cancer 97 (2007) 646–653.

[174] D. Khaitan, S. Chandna, M.B. Arya, B.S. Dwarakanath, Establishment and characterization of multicellular spheroids from a human glioma cell line; implications for tumor therapy, J. Transl. Med. 4 (2006) 12–25.

[175] A.M. Stein, T. Demuth, D. Mobley, M. Berens, L.M. Sander, A mathematical model of glioblastoma tumor spheroid invasion in a three-dimensional in vitro experiment, Biophys. J. 92 (2007) 356–365.

[176] M.A. Castro, F. Klamt, V.A. Grieneisen, I. Grivicich, J.C. Moreira, Gompertzian growth pattern correlated with phenotypic organization of colon carcinoma, malignant glioma and non-small cell lung carcinoma cell lines, Cell Proliferation 36 (2003) 65–73.

[177] J.T. Erler, K.L. Bennewith, M. Nicolau, N. Dornh ́ofer, C. Kong, Q.T. Le, J.T.A. Chi, S.S. Jeffrey, A.J. Giaccia, Lysyl oxidase is essential for hypoxia-induced metastasis, Nature 440 (2006) 1222–1226.

[178] B. Kaur, F.W. Khwaja, E.A. Severson, S.L. Matheny, D.J. Brat, E.G. Van Meir, Hypoxia and the hypoxia-inducible-factor pathway in glioma growth and angiogenesis, Neuro-Oncology 7 (2005) 134–153.

[179] J. Daruwalla, C. Christophi, Hyperbaric oxygen therapy for malignancy: A review, World J. Surg. 30 (2006) 2112–2131.

[180] E.J. Hall, A.J. Giaccia, et al., Radiobiology for the Radiologist, Lippincott Williams & Wilkins, Philadelphia, 2009.

[181] S. Kizaka-Kondoh, M. Inoue, H. Harada, M. Hiraoka, Tumor hypoxia: A target for selective cancer therapy, Cancer Science 94 (2005) 1021–1028.

[182] K. De Jaeger, M.C. Kavanagh, R.P. Hill, Relationship of hypoxia to metastatic ability in rodent tumours, Br. J. Cancer 84 (2021) 1280–1285.

[183] O. Keunen, M. Johansson, A. Oudin, M. Sanzey, S.A.A. Rahim, F. Fack, F. Thorsen, T. Taxt, M. Bartos, R. Jirik, H. Miletic, J. Wang, D. Stieber, L. Stuhr, I. Moen, C.B. Rygh, R. Bjerkvig, S.P. Niclou, Anti–VEGF treatment reduces blood supply and increases tumor cell invasion in glioblastoma, Proc. Natl. Acad. Sci. USA 108 (2011) 3749–3754.

[184] K. Lamszus, P. Kunkel, M. Westphal, Invasion as limitation to antiangiogenic glioma therapy, Acta Neurochir. Suppl. 88 (2003) 169–177.

[185] E.K. Rofstad, E. Halsør, Hypoxia-associated spontaneous pulmonary metastasis in human melanoma xenografts: Involvement of microvascular hot spots induced in hypoxic foci by interleukin 8, Br. J. Cancer 86 (2002) 301–308.

[186] O. Ilina, G.-J. Bakker, A. Vasaturo, R.M. Hoffman, P. Friedl, Two-photon laser-generated microtracks in 3D collagen lattices: Principles of MMP–dependent and –independent collective cancer cell invasion, Phys. Biol. 8 (2011) 015010.

[187] H.J.J. Bernsen, A.J. van der Kogel, Antiangiogenic therapy in brain tumor models, J. Neuro-oncol. 45 (1999) 247–255.

[188] H.J. Bloemendal, T. Logtenberg, E.E. Voest, New strategies in anti-vascular cancer therapy, Eur. J. Clin. Invest. 29 (1999) 802–809.

[189] R.K. Jain, Normalizing tumor vasculature with anti-angiogenic therapy: A new paradigm for combination therapy, Nature Med. 7 (2001) 987–989.

[190] T.T. Lah, M.B.D. Alonso, C.J.F. van Noorden, Antiprotease therapy in cancer: Hot or not? Exp. Opin. Biol. Ther. 6 (2006) 257–279.

[191] A.L. Harris, Hypoxia–A key regulatory factor in tumour growth, Nat. Rev. Cancer 2 (2002) 38–47.

[192] M.D. Brooks, M.L. Burness, M.S. Wicha, Therapeutic implications of cellular heterogeneity and plasticity in breast cancer, Cell Stem Cell 17 (2007) 260–271.

[193] C.F. Gao, Q. Xie, Y.L. Su, J. Koeman, S.K. Khoo, M. Gustafson, B.S. Knudsen, R. Hay, N. Shinomiya, G.F. Vande Woude, Proliferation and invasion: Plasticity in tumor cells, Proc. Natl. Acad. Sci. USA 102 (2005) 10528–10533.

[194] J. Hausser, U. Alon, Tumour heterogeneity and the evolutionary trade-offs of cancer, Nat. Rev. Cancer 20 (2020) 247–257.

[195] A. Roesch, Tumor heterogeneity and plasticity as elusive drivers for resistance to MAPK pathway inhibition in melanoma, Oncogene 34 (2015) 2951–2957.

[196] J. Varga, T. De Oliveira, F.R. Greten, The architect who never sleeps: Tumor-induced plasticity, FEBS Lett. 588 (2014) 2422–2427.

[197] T.A. Ulrich, E.M. De Juan Pardo, S. Kumar, The mechanical rigidity of the extracellular matrix regulates the structure, motility, and proliferation of glioma cells, Cancer Res. 69 (10) (2009) 4167–4174.

[198] G.A. Dunn, T. Ebendal, Contact guidance on oriented collagen gels, Exp. Cell Res. 111 (1978) 475–479.

[199] D. Lehnert, B. Wehrle-Haller, C. David, U. Weiland, C. Ballestrem, B.A. Imhof, M. Bastmeyer, Cell behaviour on micropatterned substrata: Limits of extracellular matrix geometry for spreading and adhesion, J. Cell Sci. 117 (1) (2004) 41–52.

[200] R.A. Gatenby, E.T. Gawlinski, A.F. Gmitro, B. Kaylor, R.J. Gillies, Acid-mediated tumor invasion: A multidisciplinary study, Cancer Res. 66 (2006) 5216–5223.